

Simultaneous Quantum Information Transfer and Quantum Operations in Quantum Dot Arrays Mediated by Spin-Orbit Interaction

D. Fernández-Fernández,^{1,*} Yue Ban,² and G. Platero¹

¹*Instituto de Ciencia de Materiales de Madrid ICMM-CSIC, 28049 Madrid, Spain.*

²*Departamento de Física, Universidad Carlos III de Madrid, Avda. de la Universidad 30, 28911 Leganés, Spain*

Quantum information transfer is fundamental for scalable quantum computing in any potential platform and architecture. Hole spin qubits, owing to their intrinsic spin-orbit interaction (SOI), promise fast quantum operations which are fundamental for the implementation of quantum gates. Yet, the influence of SOI in quantum transfer protocols remains an open question. Here, we investigate, using Shortcuts to Adiabaticity, the long-range transfer of hole spin states and quantum distribution of entangled pairs in a semiconductor quantum dot array. We demonstrate that electric field manipulation allows dynamical control of the SOI, enabling simultaneous implementation of quantum gates during the transfer, with the potential to significantly accelerate quantum algorithms. By harnessing the ability to perform quantum gates in parallel with the transfer, we employ dynamical decoupling schemes to focus and preserve the spin state, leading to higher transfer fidelity.

In the late nineties, Loss and Divizzeno proposed semiconductor quantum dots (QDs) networks as a platform for a quantum computer [1, 2]. For almost a decade, the research focused on achieving one- and two-qubit operations in GaAs single and double QDs [3–6] and on how to mitigate charge and spin decoherence in these systems [7], a critical concern in quantum computing. Hereafter, the development of quantum dots arrays (QDAs) [8–12] marked a significant step toward scalability, opening doors to new functionalities with applications in quantum computation, quantum information, and quantum simulation [13–18].

Triple quantum dots (TQDs) arranged linearly exhibit direct transport of electron spin states between outer dots, effectively using a QDA as a spin bus [19, 20]. In parallel, direct charge transfer between outer dots has been observed in photoassisted tunneling experiments within a closed TQD system [21]. Additionally, theoretical investigations have explored long-range photoassisted tunneling in TQDs [22–24]. The direct transfer of particles between distant sites with a minimal population in the intermediate dots is also known as long-range transfer.

Recent years have witnessed the implementation of longer QDAs for both electrons [25–30] and holes [31, 32], to increase the number of qubits and the complexity of quantum operations. However, existing devices often lack high connectivity between qubits, a critical hurdle in simulating more complex systems. To increase the number of problems that can be addressed with a quantum chip, the use of more dense architectures is desirable. To address the challenge of signal fan-out [33, 34], reducing the number of input terminals through a crossbar network [35, 36] has been proposed as a solution. Another approach to scalability is the use of sparse QDAs, eliminating qubit crosstalk and enabling integrated classical electronics [37]. In this architecture, distant elements within a quantum chip are connected via quantum links

or couplers, facilitating the exchange of information between computing nodes [38–40]. Various coupler options include electromagnetic cavities [41], particle shuttling via surface acoustic waves [42], bucket bridge mode [43–45], or conveyor mode [46–49].

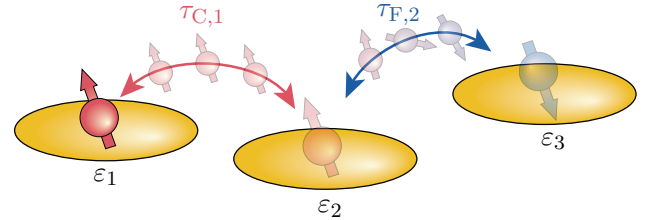


Figure 1. Schematic picture of a TQD populated with a single heavy hole. Each energy level of the dot is defined with the parameter ε_i . The particle can tunnel between adjacent dots i and $i + 1$ with a spin-conserving rate $\tau_{C,i}$. Due to the finite SOI, the particle can also tunnel to its neighboring dots with a spin-flip probability $\tau_{F,i}$.

In this work, we investigate QDAs as quantum links between elements of a quantum chip, enabling coherent quantum information transfer between the outer dots due to the presence of dark states (DSs) [50–53]. Despite considerable interest in long-range transfer protocols, the advantages of performing quantum spin transfer in materials with strong intrinsic spin-orbit interaction (SOI) [54–62] remain relatively unexplored. Most research has treated SOI as a source of decoherence during transfer [63], although it can be advantageous for achieving high-fidelity quantum gates [64]. In the present work, we explore the direct long-range transfer of quantum information in QDAs under the influence of SOI. We achieve a fast and robust entanglement distribution, a crucial element for distributed quantum computing. Furthermore, we propose a protocol for transferring electron or hole spins while simultaneously performing universal one-qubit gates. Importantly, by controlling the effects of

SOI, we demonstrate how to implement dynamical decoupling schemes alongside the transfer process, enhancing fidelity. The results presented here are valid for multi-particle systems. We obtain a fast protocol to distribute entangled pairs in a QDA and perform long-range spin transfer in a half-filling regime.

To control the transfer, we employ shortcuts to adiabaticity (STA) protocols [65], which efficiently accelerate adiabatic processes and enable high-fidelity transfer [51, 52]. Our results are valid for electron or hole spins in planar QDAs in different semiconductor materials, such as germanium or silicon, and can be extended to other semiconductor QDA implementations as quantum dots in nanowires [66]. However, our primary focus is on hole spin qubits, where the intrinsic high SOI plays an important role [67], allowing for rapid coherent spin rotations through electric dipole spin resonance [68].

Theoretical model: We consider a linear QDA with a total of N sites, populated with heavy holes (HH) with nearest-neighbor couplings, described by an Anderson-Hubbard model ($\hbar = 1$) [69]

$$H = H_0 + H_\tau + H_{\text{SOI}}. \quad (1)$$

The original Hamiltonian reads

$$H_0 = \sum_i \varepsilon_i n_i + U \sum_i n_{i\uparrow} n_{i\downarrow} + E_Z \sum_i (n_{i\uparrow} - n_{i\downarrow}), \quad (2)$$

where ε_i is the onsite energy of the dot i -th dot with $i = \{1, 2, \dots, N\}$, U is the Coulomb repulsion on each dot, and $E_Z = g\mu_B B$ the Zeeman splitting given by external magnetic field. The second term Eq. (1) represents the spin-conserving tunneling between nearest-neighbor QDs as

$$H_\tau = - \sum_{i,\sigma} \left(\tau_{C,i} a_{i\sigma}^\dagger a_{i+1\sigma} + \text{h.c.} \right). \quad (3)$$

Here, $a_{i\sigma}$ ($a_{i\sigma}^\dagger$) is the fermionic annihilation (creation) operator at site i with spin $\sigma = \uparrow, \downarrow$, and $\tau_{C,i}$ the spin-conserving tunneling rate between the i -th and the $i+1$ -th QDs. The intradot valley split is assumed to be high enough, so we only consider one orbital per dot. The last term in Eq. (1) models the SOI present for holes in semiconductor QDs. We consider holes in Si or Ge, which

present Rashba SOI [70–75]

$$H_{\text{SOI}} = i\alpha(\sigma_+ \pi_-^3 - \sigma_- \pi_+^3). \quad (4)$$

The canonical momentum reads $\boldsymbol{\pi} = \mathbf{p} + e\mathbf{A}$, and the ladder operators are defined as $\pi_\pm = \pi_x \pm i\pi_y$ and $\sigma_\pm = (\sigma_x \pm i\sigma_y)/2$, with $\sigma_{x,y,z}$ the Pauli matrices. Following [73], we obtain the matrix elements for the spin-flip tunneling rates as

$$\begin{aligned} \langle i \uparrow | H_{\text{SOI}} | i+1 \downarrow \rangle &= -\tau_{F,i}, \\ \langle i \downarrow | H_{\text{SOI}} | i+1 \uparrow \rangle &= \tau_{F,i}^*. \end{aligned} \quad (5)$$

Other elements can be obtained by imposing hermiticity on the total Hamiltonian. The SOI term can be written in terms of the spin-flip tunneling rates between nearest neighbors as

$$H_{\text{SOI}} = - \sum_i \left(\tau_{F,i}^* a_{i\uparrow}^\dagger a_{i+1\downarrow} - \tau_{F,i} a_{i\downarrow}^\dagger a_{i+1\uparrow} + \text{h.c.} \right). \quad (6)$$

Without loss of generality, we restrict ourselves to real tunneling rates $\tau_{C,i}, \tau_{F,i} \in \mathbb{R}$ (see the supplemental material for more details on the calculation of the spin-flip tunneling rate). In the following sections, the shuttling protocol will be based on the dynamical control of the tunneling rates, both spin-conserving $\tau_{C,i}(t)$ and spin-flip $\tau_{F,i}(t)$.

Dark states in a Triple Quantum Dot: Our aim is the long-range transfer of one hole spin qubit across a linear QDA. In order to reduce relaxation and dephasing effects, we investigate the direct transfer of the qubit from the leftmost to the rightmost site, reducing as much as possible the population in the intermediate dots. The minimal system for direct transfer is a TQD array populated with a single HH, as schematically shown in Fig. 1.

In order to obtain a direct hole spin transfer, we fix the QDs energy levels at $\varepsilon_i = 0$. With no magnetic field applied to the system, the spin energy levels are degenerated. We search for zero-energy modes that directly connect the edge dots of the chain with no population in the middle dot. These coherent superpositions are termed dark states (DSs). By exact diagonalization of the total Hamiltonian (see the supplemental material), and defining x_{SOI} as the ratio between spin-flip and the spin-conserving tunneling rates: $x_{\text{SOI}} \equiv \tau_{F,i}/\tau_{C,i}$ [72, 76], we find two DSs which read:

$$\begin{aligned} |\text{DS}_1\rangle &= \sin\theta |\uparrow, 0, 0\rangle - \frac{\cos\theta}{x_{\text{SOI}}^2 + 1} \left[(1 - x_{\text{SOI}}^2) |0, 0, \uparrow\rangle + 2x_{\text{SOI}} |0, 0, \downarrow\rangle \right], \\ |\text{DS}_2\rangle &= \sin\theta |\downarrow, 0, 0\rangle + \frac{\cos\theta}{x_{\text{SOI}}^2 + 1} \left[(1 - x_{\text{SOI}}^2) |0, 0, \downarrow\rangle + 2x_{\text{SOI}} |0, 0, \uparrow\rangle \right], \end{aligned} \quad (7)$$

where we have defined $\tan\theta \equiv \tau_{C,2}/\tau_{C,1}$. At the start of

the transfer protocol, the system is initialized in a DS by

populating only the leftmost QD, i.e., $\tau_{C,1} \ll \tau_{C,2}$. The particle can be adiabatically transferred to the rightmost QD by tuning the ratio between the tunneling rates, until $\tau_{C,1} \gg \tau_{C,2}$.

For simplicity, during the rest of this section, we will focus on $|\text{DS}_1\rangle$ in Eq. (7), but similar results can be obtained considering $|\text{DS}_2\rangle$. Note that any linear combination of $|\text{DS}_1\rangle$ and $|\text{DS}_2\rangle$ is also a zero-energy eigenvalue of the total Hamiltonian, so the initial state of the particle can be any superposition of spin up and spin down.

The DS connects both ends of the QDA with different weights on each spin projection, which are determined by x_{SOI} . Setting $x_{\text{SOI}} = 1$ we obtain a DS,

$$|\text{DS}_1(x_{\text{SOI}} = 1)\rangle = \sin\theta |\uparrow, 0, 0\rangle - \cos\theta |0, 0, \downarrow\rangle. \quad (8)$$

where, by tuning θ from $\pi/2$ to 0, the spin is inverted during the transfer. Another interesting choice for x_{SOI} , which can be externally controlled by electric fields, is $x_{\text{SOI}} = \sqrt{2} - 1$. In this case, the final state after the long-range transfer is a superposition with equal probability for each spin projection

$$\begin{aligned} |\text{DS}_1(x_{\text{SOI}} = \sqrt{2} - 1)\rangle &= \sin\theta |\uparrow, 0, 0\rangle \\ &\quad - \cos\theta/\sqrt{2}(|0, 0, \uparrow\rangle + |0, 0, \downarrow\rangle). \end{aligned} \quad (9)$$

Transfer Protocols: In this section, we investigate different protocols to transfer a hole spin in a TQD while inverting its spin. The system is initialized in the state $|\Psi(t=0)\rangle = |\uparrow, 0, 0\rangle$. We fix the SOI so that $x_{\text{SOI}} = 1$. This condition will be relaxed later to explore the effects of SOI on the transfer. We compare each protocol through their fidelity, which is defined as the final population of the rightmost QD with a spin-down particle $\mathcal{F} \equiv |\langle 0, 0, \downarrow | \Psi(T) \rangle|^2$, where T represents the total time of the protocol. The maximum population of the middle dot is given by $P_2 \equiv \max(\sum_{\sigma} |\langle 0, \sigma, 0 | \Psi(t) \rangle|^2)$.

One of the simplest protocols for the transfer of a single HH consists of two linear ramps at tunneling rates given by

$$\begin{aligned} \tau_{C,1}(t) &= \frac{\tau_0}{T}t, \\ \tau_{C,2}(t) &= \tau_0 - \frac{\tau_0}{T}t, \end{aligned} \quad (10)$$

where τ_0 represents the maximum tunneling rate. An illustrative example of pulse shapes can be seen in Fig. 2 (a). It is worth noting that spin-flip tunneling rates also evolve with time, following $\tau_{F,i}(t) = x_{\text{SOI}}\tau_{C,i}(t)$.

Another protocol of great interest in the literature for quantum control is coherent transfer by adiabatic passage (CTAP) [50, 51]. In CTAP, pulses are defined by Gaussian shapes as follows

$$\tau_{C,1(2)} = \tau_0 \exp\left(-\frac{(t - T/2 \mp \sigma_{\text{CTA}})^2}{\sigma_{\text{CTA}}^2}\right), \quad (11)$$

where σ_{CTA} is a free parameter that determines the standard deviation of the control pulse, with the pulse shape depicted in Fig. 2 (b).

To enhance long-range transfer, we explore STA schemes [65, 77]. In this work, we adopt the inverse engineering protocol (IE). In the IE framework, we propose an ansatz for the state evolution and analytically solve the time-dependent Schrödinger equation to obtain the pulse shapes that should be applied for the transfer. Crucially, our ansatz allows for the controlled population in the middle dot at intermediate times, with the maximum population tuned through the pulse strength. The ansatz for the wave function reads

$$\begin{aligned} |\Psi(t)\rangle &= \cos\eta \cos\chi |\uparrow, 0, 0\rangle - \sin\chi \cos\eta |0, 0, \downarrow\rangle \\ &\quad + i\frac{\sin\eta}{\sqrt{2}}(|0, \uparrow, 0\rangle + |0, \downarrow, 0\rangle), \end{aligned} \quad (12)$$

where η and χ are some auxiliary time-dependent functions. Without loss of generality, we fixed $x_{\text{SOI}} = 1$ for the above ansatz. We will see later that the pulses obtained with IE are valid for arbitrary values of x_{SOI} . By introducing Eq. (12) into the time-dependent Schrödinger equation $i\partial_t |\Psi(t)\rangle = H(t) |\Psi(t)\rangle$ we obtain the following expressions

$$\begin{aligned} \tau_{C,1}(t) &= (\dot{\eta} \cos\chi + \dot{\chi} \cot\eta \sin\chi)/\sqrt{2}, \\ \tau_{C,2}(t) &= (-\dot{\eta} \sin\chi + \dot{\chi} \cot\eta \cos\chi)/\sqrt{2}. \end{aligned} \quad (13)$$

The boundary conditions for the required initial and final states are $\eta(0) = \eta(T) = \chi(0) = 0$, and $\chi(T) = \pi/2$. We can also impose smooth pulses by using additional boundary conditions in derivatives $\dot{\chi}(0) = \dot{\chi}(T) = \ddot{\chi}(0) = \ddot{\chi}(T) = \dot{\eta}(0) = \dot{\eta}(T) = 0$. We use a common choice for smooth pulses, a Gutman 1-3 trajectory, which consists of a linear term and the two lowest odd Fourier components. The explicit expressions for the auxiliary functions are

$$\begin{aligned} \chi(t) &= \pi \frac{t}{2T} - \frac{1}{3} \sin\left(\frac{2\pi t}{T}\right) + \frac{1}{24} \sin\left(\frac{4\pi t}{T}\right), \\ \eta(t) &= \arctan(\dot{\chi}/\alpha_0), \end{aligned} \quad (14)$$

where α_0 is an arbitrary constant controlling both the maximum pulse strength $\tau_0 \propto \alpha_0$ and the total population in the middle dot $P_2(t) \equiv \sin^2 \eta(t)$. An example of pulse shapes is shown in Fig. 2 (c).

The coefficients for each Fourier component in Eq. (14) can be fine-tuned to minimize the population in the intermediate dot. Employing more Fourier components enhances transfer fidelity at the cost of more intricate pulse shapes. However, optimizing these parameters requires an exhaustive search and falls outside the scope of this work.

The maximum population in the middle dot occurs at the midpoint of the transfer and is given by

$$P_2 \equiv P_2(T/2) = \frac{(4\pi/3)^2}{(4\pi/3)^2 + T^2\alpha_0^2}. \quad (15)$$

When the total protocol time is significantly short, compared to the maximum pulse strength $T\alpha_0 \ll 1$, the middle dot is maximally populated $P_2 \rightarrow 1$. In such a case, the adiabatic condition cannot be fulfilled, but the precise engineering of pulses obtained with IE ensures that the system ends in the desired final state. To reduce the middle dot population, longer total times or stronger pulses must be used.

We compute the evolution with the total Hamiltonian given in Eq. (1), accounting for the time-dependent tunneling rates dictated by each protocol. Subsequently, we calculate the overlap between the time-dependent wave function and the DS during the transfer and define the fidelity as the overlap with the DS at $t = T$. The results for different total times are depicted in Fig. 2 (d-f). Since all protocols start with $\tau_{C,2} \gg \tau_{C,1}$, the initial state $|\uparrow, 0, 0\rangle$ corresponds to the DS in the limit $t \rightarrow 0$, which produces an overlap close to one at early times.

Fig. 2 (d) shows that by using linear ramp pulses, the overlap remains close to one for all the total times examined here. The most significant deviation from the DS during the transfer occurs in the middle of the protocol, around $t \sim T/2$. This behavior is observed as well in all the other protocols. As the dynamics approaches the adiabatic limit at longer times, the state remains in the DS, reducing the total middle dot population and achieving complete transference to the third QD. However, even if the overlap is close to one, the oscillatory behavior of the overlap makes linear ramps highly sensitive to the total transfer time. A slight deviation in time results in substantial differences in transfer fidelity. When using CTAP pulses (Fig. 2 (e)), and for the imposed transfer times, the overlap with the DS drops in the middle of the protocol, but it recovers at later times. If the imposed transfer time is too short, the drop is too severe, making it impossible to achieve high-fidelity transfers. On the other hand, the STA protocol (Fig. 2 (f)) behaves qualitatively similar to CTAP for shorter times $t < T/2$. However, due to the precise engineering of the pulses, STA consistently achieves a perfect overlap with the DS at the end of the protocol, regardless of the total time of the protocol. This results in high robustness against timing errors.

The state transfer mediated by DSs can be extended to arrays larger than three, provided that the QDA has an odd number of sites [50–52]. The transfer for $N > 3$ can be obtained using the tunneling sequence of straddling pulses [50, 78, 79]. This sequence consists of a pulse in the tunneling rates between the first and second sites and between the last two sites, similar to what we have seen before. However, the barriers between the middle dots, also known as bulk, are raised and lowered simultaneously with a time-dependent function such as $\tau_{C,i} = \tau_s \exp(-(t - T/2)^2 / (2\sigma_{\text{bulk}}^2))$ with $1 < i < N - 1$ and τ_s being the maximum value for the straddling pulses. If we impose large straddling pulses $\tau_s \gg T_0$,

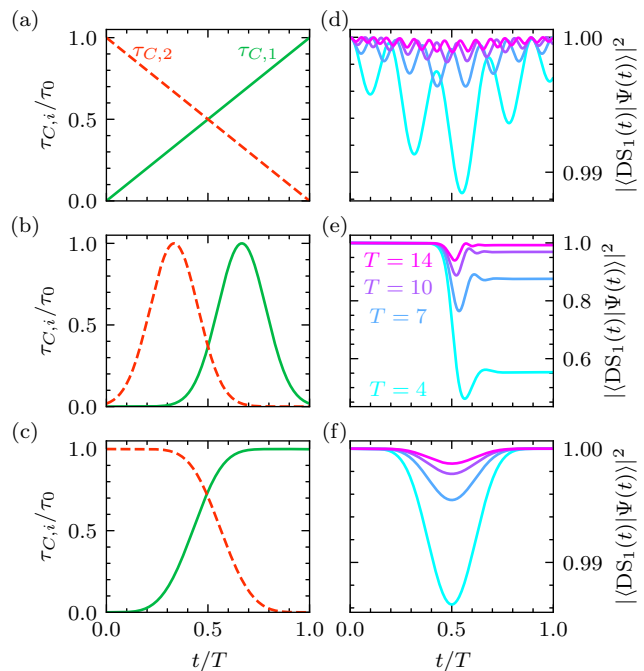


Figure 2. (a-c) Pulse shapes for (a) linear ramps, (b) CTAP, and (c) STA. (d-f) Overlap between the dark state $|\text{DS}_1(t)\rangle$ and the time-dependent wave function $|\Psi(t)\rangle$ during the state transfer implemented with (d) linear ramps, (e) CTAP, and (f) STA. The colors for the right column represent the total time of the protocol in units of $[2\pi/\tau_0]$, shown in (e). Note that the y axis scale for the right column is different for each protocol.

the system can be reduced to a three-site system with renormalized tunneling rates $\tau'_{C,1} = -\tau_{C,1}/\sqrt{(N-1)/2}$ and $\tau'_{C,2} = (-1)^{(N-1)/2}\tau_{C,N-1}/\sqrt{(N-1)/2}$, and similarly, with renormalized spin-flip tunneling rates $\tau'_{F,1}$ and $\tau'_{F,2}$ (see the supplemental material for more information about how to obtain the effective model). These two pulses are usually referred to as pump and Stokes pulses, respectively.

To benchmark the long-range transfer protocols discussed above, we compare them with the traditional sequential transfer protocol, also known as the bucket-brigade mode, where the tunneling rates between all neighboring dots are maintained at a constant value, and the driving parameter is the detuning between QDs. Initially, the particle is trapped in one QD due to a significant detuning from neighboring dots. Subsequently, the detuning is gradually reduced until the ground state corresponds to the particle being trapped in the neighboring dot. If this ramp is sufficiently slow (adiabatic) the particle is sequentially transferred from one QD to its neighbor, reaching the final site after a total of $N - 1$ sequences. Here, we define the maximum value of the detuning as ε_{max} , and the minimum value, without loss of generality, as $\varepsilon_{\text{min}} = 0$.

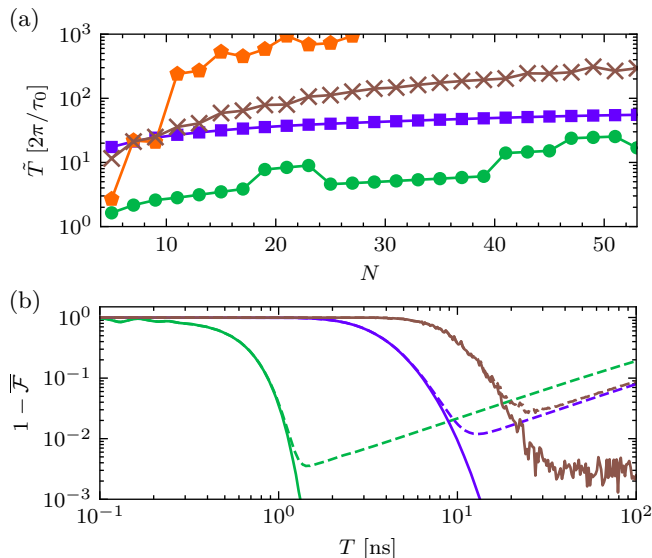


Figure 3. (a) Time needed to reach a 99% fidelity for different protocols, versus the number of sites in the QDA. The transfer is obtained via a sequential transfer (crosses, brown), a linear pulse (pentagons, orange), CTAP (squares, purple), and STA (circles, green). The maximum tunneling rates are $\tau_s = 3\tau_0$, and for the sequential transfer $\varepsilon_{\max} = 20\tau_0$. (b) Transfer infidelity as a function of the total protocol time for different protocols for a seven QDA. The solid lines represent the results in the absence of dephasing, while the dashed lines represent the results for $\gamma = 0.1 \mu\text{eV}$. The maximum tunneling rates are $\tau_s = 10\tau_0 = 100 \mu\text{eV}$. For the sequential transfer $\varepsilon_{\max} = 500 \mu\text{eV}$. Other parameters, common for both panels, $\sigma_{\text{CTAP}} = \sigma_{\text{bulk}} = T/6$.

We define \tilde{T} as the minimal protocol time needed to obtain a quantum state transfer with fidelity of $\mathcal{F} = 99\%$. In Fig. 3 (a), we show the results for different protocols versus the number of sites in the QDA. The total time needed using a linear ramp grows exponentially with the number of sites. On the contrary, an STA pulse reaches a high-fidelity transfer with moderate times. For very large arrays, the CTAP and STA protocols approach each other. Since the straddling pulses in the bulk are the same for both protocols, this result is expected. However, this assumption can not be extrapolated to linear pulses, where the time necessary to achieve a 99% fidelity abruptly increases with the length of the chain as compared with the other protocols. Both STA and CTAP outperform sequential transfer, demonstrating the superiority of employing long-range transfer in long chains. Furthermore, as shown in Fig. 3 (a), STA is much faster than CTAP.

Another advantage of long-range transfer is the reduction of the effects of pure dephasing. To simulate this effect we solve the Lindblad master equation [80] with jump operators $L_i = \sqrt{\gamma_i}\sigma_z^i$, where γ_i is the dephasing rate for the i -th QD. We assume all QDs have the same

dephasing rate $\gamma_i = \gamma$. We compute the fidelity $\overline{\mathcal{F}}$ as the average of the transfer fidelity for different initial spin polarization. In Fig. 3 (b), we show the fidelity as a function of the dephasing rate γ for different protocols. Since long-range transfer protocols do not populate the intermediate dots, the fidelity is less affected by dephasing, obtaining a higher fidelity for the same dephasing rate. The advantage of STA or CTAP over sequential transfer is more evident for higher dephasing rates and longer QDAs.

Spin control: Let us perform a detailed analysis of DSs in a chain with an odd number of QDs, $N = 2k + 1$, where $k \in \mathbb{N}$. In the limit $\tau_s \gg \tau_0$, we derive a solution as follows:

$$\begin{aligned} |\text{DS}_1\rangle &= \sin\theta |\uparrow_1\rangle - \cos\theta [\cos\vartheta/2 |\uparrow_N\rangle + \sin\vartheta/2 |\downarrow_N\rangle], \\ |\text{DS}_2\rangle &= \sin\theta |\downarrow_1\rangle - \cos\theta [-\sin\vartheta/2 |\uparrow_N\rangle + \cos\vartheta/2 |\downarrow_N\rangle]. \end{aligned} \quad (16)$$

Here, the mixing angle between spin states at the last site is given by

$$\vartheta \equiv 2(N-1) \arctan(x_{\text{SOI}}). \quad (17)$$

This outcome reveals the dependence of the spin polarization of the transferred particle on the number of QDs in the array and on the strength of the SOI, which can be modulated through external electric fields. For the case of $N = 3$, the spin is inverted in the transfer for $x_{\text{SOI}} = 1$. In contrast, spin-conserving transfer occurs at $x_{\text{SOI}} = 0$, where the SOI is zero. In Fig. 4 (a), simulations of the spin polarization at the rightmost QD after a long-range transfer carried out with STA are shown. The values of x_{SOI} that yield long-range spin-conserving and spin-flip transfers are in agreement with the analytical results discussed earlier.

For $N = 5$, solutions for a spin-flip transfer ($\vartheta = (2k+1)\pi$) emerge at $x_{\text{SOI}} = \sqrt{2} \pm 1$. On the other hand, for a spin-conserving transfer ($\vartheta = 2k\pi$), there are three possible solutions. These correspond to the absence of SOI $x_{\text{SOI}} = 0$, equal spin-conserving and spin-flip tunneling rates $x_{\text{SOI}} = 1$, and absence of spin-conserving tunneling rate $x_{\text{SOI}} \rightarrow \infty$. Similar outcomes are expected for higher N values. These predictions are closely aligned with the numerical results presented in Fig. 4 (b-c).

In addition, we simulate various chain lengths for long-range transfer using an STA protocol and compute the final polarization defined as $\mathcal{P} \equiv |\langle \uparrow_N | \Psi(T) \rangle|^2 - |\langle \downarrow_N | \Psi(T) \rangle|^2$. As in previous cases, the system is initialized in the state $|\uparrow_1\rangle$. The results are displayed in Fig. 4 (d), where blue regions ($\mathcal{P} = -1$) represent spin-flip transfers, while red ones ($\mathcal{P} = 1$) indicate spin-conserving ones. These analyses are limited to chains with an odd number of QDs since only these systems exhibit dark states. As described in supplemental material, the effective tunneling rates decrease as $1/\sqrt{(N-1)/2}$

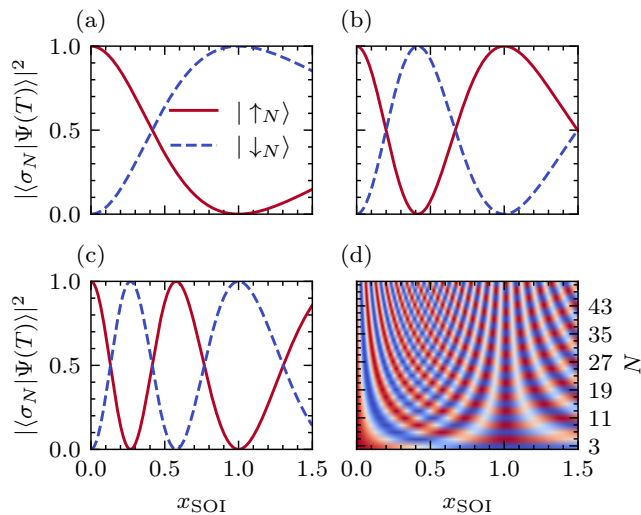


Figure 4. Population of the rightmost dot after a long-range transfer as a function of $x_{\text{SOI}} = \tau_{F,i}/\tau_{C,i}$ for (a) $N = 3$, (b) $N = 5$, and (c) $N = 7$. The spin is initialized at the left-most QD with spin up, and it is transferred to the right-most QD ending with spin up (solid red line), or with spin down (dashed blue line). (d) Hole spin polarization at the right-most QD at the end of the protocol as a function of x_{SOI} and N is an odd number (blue: spin down, red: spin up). The protocol used for the pump and Stokes pulses is an STA pulse, with a maximum value of $\max(\tau_{C,1}) = \max(\tau_{C,N-1}) = \tau_0\sqrt{(N-1)/2}$, while the intermediate tunneling rates are straddling pulses with Gaussian shapes centered at $T/2$, with width $\sigma_{\text{CTAP}} = \sigma_{\text{bulk}} = T/6$ and maximum strength of $\tau_s = 15\tau_0\sqrt{(N-1)/2}$. The total protocol time is $T = 20\pi/\tau_0$.

for increasing site number. To counteract this effect, we increase the pulse strength by a factor $\sqrt{(N-1)/2}$, ensuring that the effective tunneling rate remains consistent across all QDA. At $x_{\text{SOI}} = 1$, we observe the alternating behavior of the spin polarization with the number of QDs mentioned above. The results resemble an interference pattern with an increasing fringe frequency as the chain length increases.

Simultaneous one-qubit gate: As we have discussed previously, the presence of SOI produces the spin rotation of the particle during the transfer. One can tune this rotation by controlling the effective Rashba interaction. In the present setup, the spin rotation takes place around the y axis in the Bloch sphere. Consequently, the final unitary transformation, after tracing out the spatial part, can be represented as

$$R_Y(\vartheta) = \begin{pmatrix} \cos \vartheta/2 & -\sin \vartheta/2 \\ \sin \vartheta/2 & \cos \vartheta/2 \end{pmatrix}. \quad (18)$$

To determine the final rotation angle, the time-dependent Schrödinger equation is solved numerically. In Fig. 5 (a), we compare these numerical results with the analytical prediction provided in Eq. (17), showing an

excellent agreement. Here, we introduce the parameter χ_{SOI} , defined as $\chi_{\text{SOI}} \equiv (1/x_{\text{SOI}} + 1)^{-1}$.

To enable arbitrary one-qubit gates, it is imperative to have the capability for two-axis control. This requirement can be achieved by introducing an effective SOI with a complex phase. In this case, the dark states take the form

$$\begin{aligned} |\text{DS}_1\rangle &= \sin \theta |\uparrow_1\rangle - \cos \theta [\cos \vartheta/2 |\uparrow_N\rangle \\ &\quad + e^{i\varphi} \sin \vartheta/2 |\downarrow_N\rangle], \\ |\text{DS}_2\rangle &= \sin \theta |\downarrow_1\rangle - \cos \theta [-\sin \vartheta/2 |\uparrow_N\rangle \\ &\quad + e^{i\varphi} \cos \vartheta/2 |\downarrow_N\rangle]. \end{aligned} \quad (19)$$

In this context, the effective complex spin-flip tunneling rate is given by $\tau_{F,i} = |\tau_{F,i}|e^{i\varphi}$. The SOI phase determines the relative phase between the spin-up and spin-down states in the rightmost QD following the long-range transfer. As discussed in [81–84], when a periodic electric field is applied to the sample, the Rashba SOI acquires a complex phase as $\alpha = \alpha_0 e^{i\omega t + \phi}$. This driving directly translates into a time-dependent spin-flip tunneling rate $\tau_{F,i}(t) = |\tau_{F,i}(t)|e^{i\omega t + \phi}$, where ω is the driving frequency and ϕ the driving phase angle. We should note that the time-dependent SO amplitude $\alpha_0(t)$ is a result of the specific pulse protocol considered (e.g., STA, CTAP).

Due to the driving in the spin-flip tunneling rate, we can control the rotation axis through the driving frequency and phase angle. If the driving frequency is sufficiently low, the dynamics align with the DS, and the final phase between the spin-up and spin-down states after the long-range transfer is determined by $\varphi \equiv \omega T + \phi$. For $\varphi = 0$, the rotation occurs around the x -axis, while $\varphi = \pi/2$ results in rotation around the y -axis. Here, we only mention these two possibilities, but any rotation vector in the x - y plane can be chosen by modifying the driving phase. A schematic representation is provided in Fig. 5 (b).

Combining three rotations around two perpendicular axes, any one-qubit gate can be implemented [85]. Moreover, if the rotation axes can be adjusted freely within a set plane, such as the x - y plane, then achieving a one-qubit gate only requires two rotation steps [86]. In Fig. 6 (a), we show a possible implementation of a general one-qubit gate. The total QDA is divided into three subarrays, each containing three QDs. The first and third subarrays are used to implement rotations around the y -axis, while the second subarray is used to implement a rotation around the x -axis. Usual one-qubit gates times for spin qubits $T_{1\text{Q}} \sim 10 - 100$ ns [87], both for electrons and holes, are comparable with the timescales of the long-range transfer protocols presented here.

The use of simultaneous one-qubit gates in parallel with the transfer of quantum information is also advantageous for the distribution of quantum entanglement, see Fig. 6 (b). The goal is to generate entanglement between two distant qubits that are not directly coupled

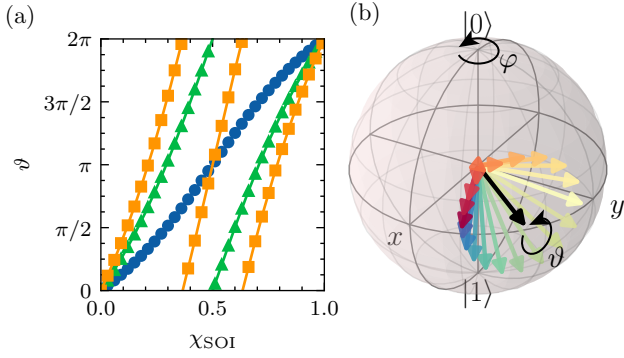


Figure 5. (a) Spin rotation angle versus the parameter χ_{SOI} . Long-range transfer is obtained using STA pulses in a QDA with a total of $N = 3$ (blue, circles), $N = 5$ (green, triangles), and $N = 7$ (orange, squares) sites. Both numerical (markers) and analytical results (solid lines) are shown. (b) Sketch of the rotation angles in the Bloch sphere. The rotation angle ϑ is given by the SOI parameter χ_{SOI} , while the rotation vector is defined via the azimuth angle φ . This angle is modified by the driving frequency of the Rashba term.

to each other. However, they are coupled to a third qubit, which can be shuttled between them, using the long-range transfer protocols discussed above. Due to the non-zero SOC, one can use the second shuttling depicted in Fig. 6 (b) to perform two quantum gates simultaneously to the transfer, speeding up the protocol. The final Bell pair between the distant qubits can be chosen via the quantum gates performed during the shuttling, while the ancilla qubit recovers its original quantum state after the protocol. In this example, outer qubits represent distant quantum cores, which are operated individually, and the ancilla qubit would denote a particle inside a quantum bus connecting both cores.

Dynamical decoupling: In experimental devices, even with isotopically purified silicon, there exists a small but finite hyperfine interaction (HFI) that can induce spin decoherence and relaxation. We model the HFI as a quasistatic Gaussian noise, which gives rise to local fluctuating magnetic fields characterized by a zero mean and a standard deviation of σ_{hf} . The timescale of the hyperfine interaction is long enough so that the random magnetic fields remain constant during the transfer. These fluctuating magnetic fields introduce errors in the transfer process and also induce dephasing in the moving spin qubit.

To improve the robustness of the protocol, we can leverage the opportunity to apply quantum gates in parallel with the transfer. We show below that it is possible to implement a dynamical decoupling protocol while transferring, and, as a proof of concept, we consider the Hahn echo protocol. The Hahn echo protocol involves a sequence of three pulses around one rotation vector. It has already been implemented in standing spin qubits

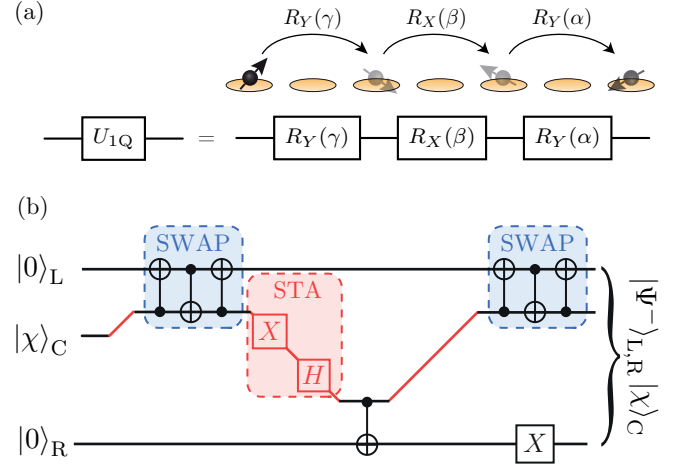


Figure 6. (a) A general one-qubit gate can be implemented by combining a maximum of three rotations around two perpendicular axes. This can be obtained by dividing the total QDA into three subarrays, so each rotation is performed in a different subarray. (b) Quantum circuit for a distributed quantum state preparation mediated by a quantum bus. The outer qubits are initialized at $|0\rangle_{L,R}$, while the initial state of the qubit inside the quantum bus (ancilla qubit) is arbitrary $|\chi\rangle_C$. The qubit inside the quantum bus is transferred via a long-range protocol (red lines). During the second transfer, two one-qubit gates (X and H) are applied to the ancilla qubit, speeding up the protocol. The final state for the outer qubits is the Bell pair $|\Psi^-\rangle_{L,R} \equiv (|0\rangle_L \otimes |1\rangle_R - |1\rangle_L \otimes |0\rangle_R) / \sqrt{2}$, and the ancilla qubit recovers its initial state.

in semiconductor QDs [44, 88, 89]. In our setup, the natural rotation axis is the y -axis. The first and third quantum gates introduce a rotation angle of $\pi/2$, while the second gate is characterized by a rotation angle of π . Ideally, after the complete sequence, the qubit returns to its initial state. A schematic representation of the dynamical decoupling protocols explained below is shown in the supplemental material.

In our system, we divide the total QDA into a total of three subarrays of length n_3 each, to perform long-range transfers. The total length of the QDA is given by $N = 3 \times n_3 - 2$, accounting for the two QDs shared between adjacent subarrays. During each transfer, the rotation angle is fixed by tuning the SOI. We refer to this method as a three-step dynamical decoupling.

However, when very long arrays are considered, the increasing number of dots in the subarrays can lead to lower quantum gate fidelity, and to address this issue, we propose an alternative approach. The total QDA is divided into five subarrays. The first, third, and fifth subarrays consist of three sites each, in which we apply the quantum gates required by the Hahn echo protocol. The remaining subarrays, the second and fourth, consist of any odd number of sites n_5 , in which the identity quantum gate are applied. The value of x_{SOI} in this region is chosen so

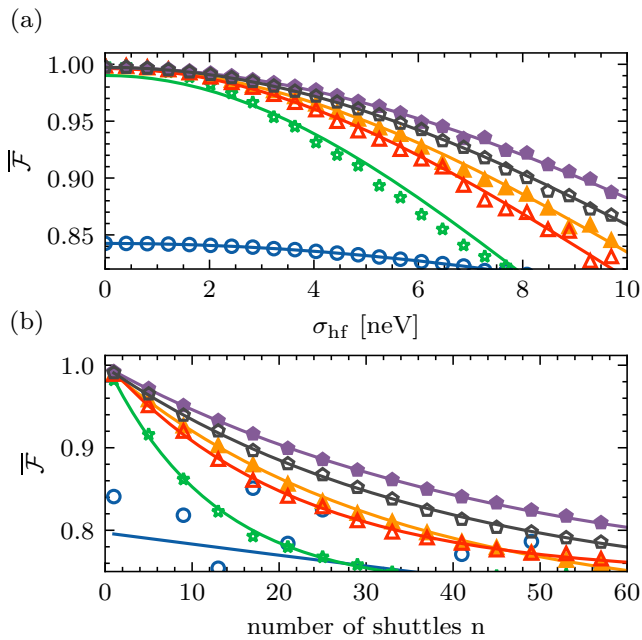


Figure 7. Average transfer fidelity for sequential (blue, circles), direct (green, stars), 3-step without DD (red, triangles), 3-step with DD (orange, full triangles), 5-step without DD (gray, pentagons), and 5-step with DD (violet, full pentagons). Each point represents an average over multiple random initial spin states and a random initialization of the Gaussian noise. In panel (a), a single shuttling is performed. In panel (b), multiple forward and reverse shuttlings are performed, while the noise strength is fixed at $\sigma_{\text{hf}} = 2$ neV. Solid lines represent fits for the numerical data, see main text. For both panels, $N = 19$, $\tau_0 = 1 \mu\text{eV}$, and $T \sim 300$ ns.

that the spin is not rotated during the transfer ($\vartheta = k\pi$). Any possible errors during the shuttlings in the second and fourth subarrays are corrected by the dynamical decoupling protocol applied in the smaller subarrays. The total length of the array is given by $N = 3 \times 3 + 2 \times n_5 - 4$, so this approach is termed five-step dynamical decoupling. Ideally, the intermediate subarrays are chosen to be as long as possible, with $n_5 \gg 3$.

To benchmark these protocols, we compare their results with those obtained by dividing the total QDA similarly but without applying quantum gates to the transferred qubit. The minimum length of the QDA that can be used to compare both proposals is $N = 19$. For all long-range transfers during the dynamical decoupling schemes, we use the STA protocol, since it is the fastest one.

The results presented in Fig. 7 (a-b) demonstrate the effectiveness of various transfer protocols. Here, we define direct transfer as the long-range transfer through the entire QDA without applying quantum gates to the transferred qubit. The spin dephasing time is given by $T_2^* = \hbar/\sigma_{\text{hf}}$ [90], and the values considered here are in line with the dephasing time observed in spin qubits [87].

We conducted multiple shuttle operations, initializing the particle in the left QD with a random spin state and averaging the transfer fidelity over different realizations of random hyperfine interactions. In particular, the fidelity obtained with multiple sequential passages remains low even in the absence of hyperfine interaction. However, this protocol exhibits increased robustness against errors because it does not rely on the energy levels being in resonance, as in the case where the protocol is based on the existence of DSs.

Direct transfer, while achieving high fidelity in the limit of low hyperfine strength, deteriorates more rapidly than sequential transfer. Dividing the total QDA into smaller subarrays enhances robustness. Furthermore, applying the dynamical decoupling sequence yields significant improvements in fidelity. These results highlight the advantage of executing quantum gates simultaneously to quantum state transfer.

To quantitatively assess the performance of dynamical decoupling protocols, we fitted the fidelity to an exponential decay of the form [47]

$$\bar{\mathcal{F}} = \frac{\mathcal{F}_0}{2} [1 + \exp(-(\sigma_{\text{hf}}/\sigma_{\text{hf}}^*)^2)], \quad (20)$$

where \mathcal{F}_0 and σ_{hf}^* are the fitting parameters. The value of σ_{hf}^* is indicative of the robustness of the protocol. In a real-case scenario, the particle must experience multiple shuttlings to connect distant quantum computing nodes, as shown in the previous example. To study the performance of the dynamical decoupling protocols in this scenario, we consider multiple forward and reverse shuttlings. Here, we fit the numerical data to an exponential decay of the form [44]

$$\bar{\mathcal{F}} = \mathcal{F}_0 \exp(-n/n^*) + \mathcal{F}_{\text{sat}}, \quad (21)$$

where n^* defines the number of shuttles after which fidelity drops to $1/e$ of its initial value, and \mathcal{F}_{sat} is the saturation value of the fidelity.

The results for the fitting parameters are shown in Table I, where we can see that the application of the dynamical decoupling sequence significantly improves the robustness. Our results show that by including a dynamical decoupling scheme during the shuttling, the qubit transfer is more robust against hyperfine interaction, and a larger number of shuttles can be performed before the fidelity significantly drops.

In practice, the successful implementation of this protocol in an experimental device requires a fast switch of the SOI. However, this can be challenging on some devices. A workaround is to take advantage of the fact that the rotation angles depend not only on the value of x_{SOI} but also on the number of sites. Setting a specific value of x_{SOI} and determining the required QDA length, we can effectively apply the dynamical decoupling sequence. For example, with $x_{\text{SOI}} \sim 0.414$, we can divide the total QDA into three sections consisting of three, five, and

	Sequential	Direct	Three-steps	Three-steps (DD)	Five-steps	Five-steps (DD)
\mathcal{F}_0	0.842	0.990	0.996	0.996	0.997	0.997
σ_{hf}^* [neV]	31.1	12.1	14.7	16.0	17.5	20.0
n^*	521	12.5	21.6	32.37	37.8	45.8

Table I. Fitting parameters (see Eqs. (20, 21)) for the sequential, direct, three- and five-steps protocols versus the noise strength and number of shuttles. The protocols in which dynamical decoupling is applied are denoted by (DD), other protocols do not include quantum gates during the shuttling.

three QDs, respectively. In this configuration, a rotation of $R_y(\pi/2)$ is applied during transfer in sections with three QDs, while the intermediate section with five QDs is subject to a quantum gate of $R_Y(\pi)$, effectively implementing the Hahn echo protocol.

Furthermore, due to the ability to perform rotations in different axes, such as the x - and y -axes, these ideas can be extended to more complex dynamical decoupling protocols, such as the Carr-Purcell-Meiboom-Gill (CPMG) scheme [91, 92]. To implement the CPMG scheme, the QDA must be divided into a minimum of four subarrays, with rotations following the sequence $R_X(\pi/2), R_Y(\pi), R_Y(\pi), R_X(\pi/2)$. Additionally, applying simultaneous quantum gates during the long-range transfer can facilitate periodic repetitions of high-order dynamical decoupling sequences, leading to stroboscopic saturation. However, implementing these advanced schemes falls beyond the scope of the present work.

Quantum state distribution: The ideas presented in this work can be extended to systems with more than one particle, with a focus on quantum state distribution. In this scenario, we aim to transfer quantum information encoded in the spin of two entangled particles. We initialize the system in a maximally entangled state, either a singlet or triplet state, which can be represented as $|T_0/S(1,1)\rangle \equiv (|\uparrow, \downarrow\rangle \pm |\downarrow, \uparrow\rangle)/\sqrt{2}$. Subsequently, we separate the entangled pair into distant sites of the QDA by tuning the tunneling rates. The schematic illustration of this idea can be found in Fig. 8 (a).

The minimal system for investigating long-range quantum state distribution with two particles, in terms of DSs, consists of a quadruple QDA. Initially, the entangled pair is located at the left-most QD and its neighbor. We consider the singlet state $|\Psi(0)\rangle = |S_{12}\rangle$, with the particles located at dots 1 and 2. Similar results can be obtained when the entangled pair is initialized in the unpolarized triplet state.

Inspired by similar protocols in Ref. [52], we use specific pulse shapes:

$$\begin{aligned} \tau_{C,1(3)} &= \mp \tau_0 \left[\tanh\left(\frac{t-b}{c}\right) \mp 1 \right], \\ \tau_{C,2} &= a\tau_0 \left[\tanh\left(\frac{t-b_2}{c}\right) + 1 \right]. \end{aligned} \quad (22)$$

Here, $a = 20$, $b = T/7$, $b_2 = 3T/5$, and $c = T/14$. Recall

that T is the total protocol time. These pulse shapes are depicted in Fig. 8 (b). The free parameters (a , b , and c) can be further fine-tuned for improved transfer robustness, although detailed parameter optimization is not within the scope of this work.

The results obtained using these pulses are displayed in Fig. 8 (c). Notably, the intermediate dot (labeled as 3) remains unpopulated during the transfer. As the time reaches $t \sim T/2$, singlet and triplet states distributed at the ends of the QDA begin to oscillate. The coupling between these states is due to the nonzero SOI. By selecting the total transfer time, a long-range distribution that preserves spin can be achieved at $t\tau_0/2\pi \sim 45$. On the other hand, if the transfer protocol ends at $t\tau_0/2\pi \sim 35$, the final state is the triplet state. In the latter case, the quantum gate applied simultaneously to the transfer effectively acts as a Z gate applied to one of the two entangled qubits.

For a more detailed analysis of the quantum state distribution, we define the final spin polarization at a given time during the transfer protocol, as follows

$$\mathcal{P}_{S(T)}(t) \equiv |\langle S(T^0)_{1,4} | \Psi(t) \rangle|^2. \quad (23)$$

Fig. 9 (a) illustrates that when the spin-flip tunneling rate is negligible (i.e., $x_{\text{SOI}} \rightarrow 0$), the distributed pair remains in the singlet state. However, as we increase the SOI to $x_{\text{SOI}} \geq 0.5$, the system starts to oscillate between the singlet and triplet states. High values of x_{SOI} lead to a higher oscillation frequency, achieving a high-fidelity state distribution at lower total times.

The final spin polarization can also be controlled by adjusting the magnetic field applied to the sample, as shown in Fig. 9 (b). If the magnetic field is not high enough, the polarized triplet states (T_{\pm}) are close in energy to the singlet and the unpolarized triplet states. The coupling to polarized triplet states acts as a leakage out of the computational basis, so the high-fidelity transfer can only be achieved if $E_Z \gg \tau_0$.

Half-filling regime: Another situation in which the presence of SOI is advantageous for the application of long-range transfer is a QDA in the half-filling regime. This situation involves a system of N sites with a total of N holes, where all QDs are in resonance and a magnetic field is applied perpendicular to the QD plane.

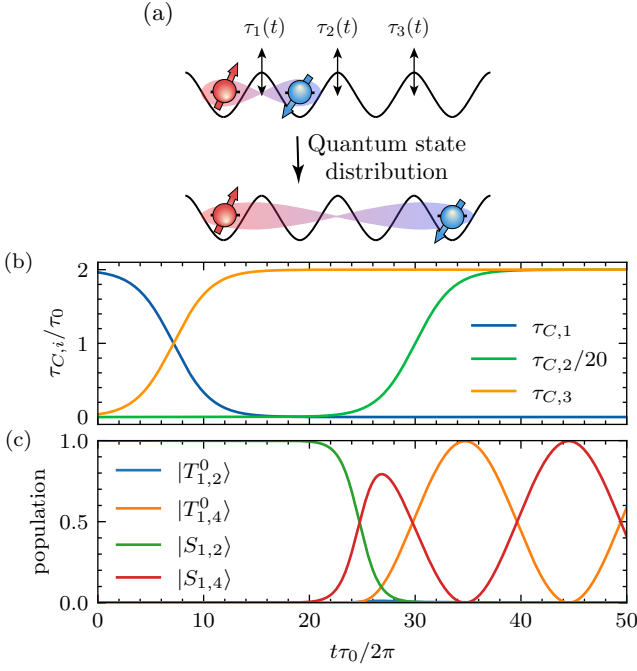


Figure 8. (a) Schematic picture of the state distribution of an entangled pair of HH across a quadruple QD, by adiabatically modifying the tunneling barriers $\tau_i(t)$. (b) Pulses used for the state distribution, note that the intermediate tunneling rate $\tau_{C,2}$ is downscaled by a factor of 20. (c) Dynamics of a quadruple QD populated with two HHs, initialized in the singlet state, after applying the pulses shown in (b). The parameters are: $x_{\text{SOI}} = 1$, $T = 50\pi/\tau_0$, $a = 20$, $b = T/7$, $b_2 = 3T/5$, $c = T/14$, $E_Z = 600\tau_0$, and $U = 2500\tau_0$.

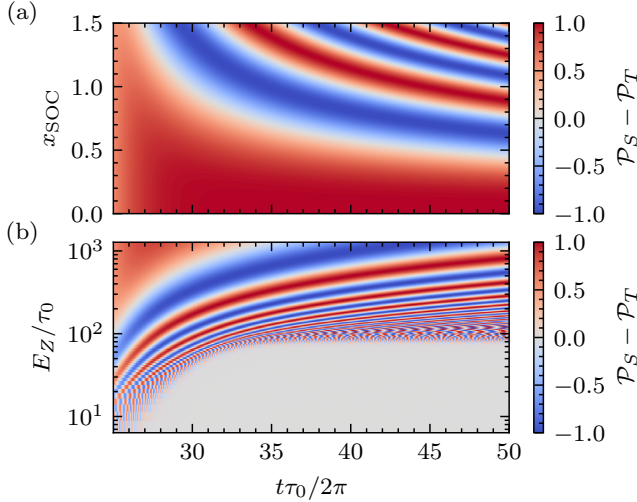


Figure 9. (a) Spin polarization $\mathcal{P}_S - \mathcal{P}_T$ in quadruple QDA after a state distribution, versus the protocol time and x_{SOI} . (b) Spin polarization versus the protocol time and Zeeman splitting E_Z . Other parameters are the same as those used in Fig. 8.

In the limit of a large Coulomb interaction, where U is

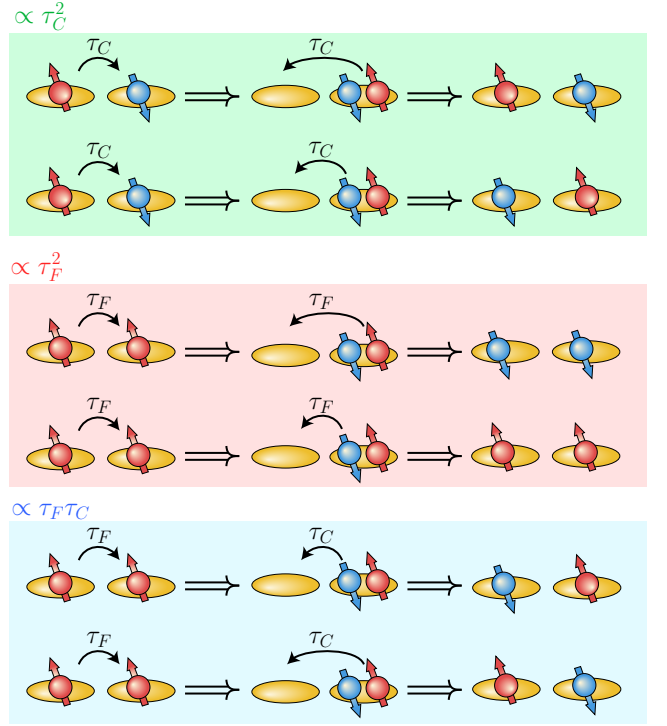


Figure 10. Different possible paths for second-order tunneling in the half-filling regime combining spin-conserving and spin-flip tunneling rates. There exist paths that are second order in the spin-conserving tunneling rate (top, green), second order in the spin-flip tunneling rate (center, pink), and a combination between spin-conserving and spin-flip tunneling rate (bottom, blue).

much larger than the other energy scales of our problem, we employ a Schrieffer-Wolff transformation to trace out the double-occupied states. In Fig. 10, we show the different possible paths for second-order tunneling processes in the half-filling regime. If the applied magnetic field is sufficiently strong $E_Z \gg \tau_{C,i}, \tau_{F,i}$, the subspaces with fixed total spin projections are separated by a considerable energy gap. In this case, the coupling between states is primarily governed by the spin-conserving tunneling rates, while the spin-flip tunneling rates renormalize the energies of each level. For more details on the effective exchange model, see the supplemental material.

The matrix representation of the effective Hamiltonian within the $S_z = +1/2$ subspace, written on the basis of $(|\downarrow, \uparrow, \uparrow\rangle, |\uparrow, \downarrow, \uparrow\rangle, |\uparrow, \uparrow, \downarrow\rangle)$, can be expressed as

$$H_{\text{eff}} = \begin{pmatrix} -J_1^{CC} - J_2^{FF} & J_1^{CC} & 0 \\ J_1^{CC} & -J_1^{CC} - J_2^{CC} & J_2^{CC} \\ 0 & J_2^{CC} & -J_2^{CC} - J_1^{FF} \end{pmatrix}. \quad (24)$$

Here, J_i^{ab} represents the exchange coupling between the dots i -th and $i+1$ -th, with $J_i^{ab} \equiv \tau_{a,i}\tau_{b,i}/U$, where $a, b = \{C, F\}$ represents the spin-conserving and spin-flip tunneling rates, respectively. A common factor E_Z

has been subtracted from the diagonal elements of the Hamiltonian. We will mainly focus on the $S_z = +1/2$ subspace, although analogous results can be applied to the $S_z = -1/2$ subspace. The effective Hamiltonian resembles a Λ system, with a central state ($|\uparrow, \downarrow, \uparrow\rangle$) coupled to the other two states. To simplify the notation, we define $|i\rangle$ as the state in which all dots are populated with a single spin-up HH, except for the i -th site where there is a spin-down HH.

For the achievement of long-range spin transfer, it is imperative to have a DS, an instantaneous eigenstate that exclusively has weight in the initial and final desired states. A condition for the existence of this DS in a Λ system is that $E_1 = E_3$, where $E_i \equiv \langle i | H_{\text{eff}} | i \rangle$ [93]. In the absence of SOI, this condition is satisfied only if $J_1^{CC} = J_2^{CC}$ at all times. However, when this condition is imposed, the DS remains constant at $|\text{DS}\rangle = (|1\rangle + |3\rangle)/\sqrt{2}$ throughout the process, without dependence on the tunneling rates, making the spin transfer unachievable.

To enable long-range spin transfer without SOI, it is necessary to apply magnetic field gradients in combination with AC driving on the tunneling barriers, wherein the pulse envelope undergoes slow changes [53]. Nonetheless, generating large magnetic field gradients could pose challenges in experimental setups, and AC fields have the potential to induce heating in the sample, leading to significant transfer errors.

These challenges can be avoided by considering holes that exhibit nonzero SOI. Setting $\tau_{F,i}/\tau_{C,i} = 1$, i.e., $J_i^{CC} = J_i^{FF} = J_i$, the Hamiltonian presented in Eq. (24), after subtracting a common factor $-(J_1 + J_2)$ in the diagonal elements, reads

$$H_{\text{eff}} = \begin{pmatrix} 0 & J_1 & 0 \\ J_1 & 0 & J_2 \\ 0 & J_2 & 0 \end{pmatrix}. \quad (25)$$

With this effective Hamiltonian, we perform an STA protocol to transfer the spin. For this purpose, we consider an ansatz for the wave function similar to the one presented in Eq. (12) to determine time-dependent pulses J_1 and J_2 to achieve long-range spin transfer of a single spin in a TQD containing three HHs. The system is initially prepared in the state $|1\rangle$. By means of STA and the DS

$$|\text{DS}\rangle = \sin \theta |1\rangle - \cos \theta |3\rangle, \quad (26)$$

where $\tan \theta \equiv J_2/J_1$, the transfer of the spin down to the rightmost end of the QDA is achieved.

It is interesting to note that the effective model is the same as that obtained for a single particle. That means that the discussion regarding the different protocols and the effects of noise are equivalent to the half-filling regime. Therefore, the results obtained for the single-particle case can be directly applied to the half-filling regime.

CONCLUSIONS

In this work, we investigate the long-range transfer of electron or hole spins in semiconductor quantum dot arrays in the presence of spin-orbit interaction (SOI). We demonstrate that the fidelity can be significantly enhanced by engineering the tunneling rates of the barriers appropriately. A detailed analysis comparing various protocols reveals that STA emerges as the optimal protocol, ensuring rapid and high-fidelity transference even in the presence of dephasing. Importantly, STA is the highest fidelity protocol for large quantum dot arrays, being therefore more suitable for scalability purposes. Furthermore, we introduce a framework to control and tune the spin rotations induced by SOI during the transfer which allows simultaneously the implementation of one-qubit quantum gates. In particular, we propose how to implement dynamical decoupling protocols to mitigate the effects of hyperfine interaction and enhance transfer fidelity. The application of simultaneous one-qubit gates during the transfer is advantageous to generate entanglement between two distant qubits. Expanding our analysis to multiparticle systems, we demonstrate that SOI presence facilitates long-range entanglement distribution across the quantum dot array. Additionally, SOI enables long-range spin transfer in the half-filling regime, a feat unattainable in the absence of SOI. The generality of our results extends to spin qubits in different semiconductor materials, such as germanium or silicon, in nanowires, and FinFET devices, as well as to electronic systems featuring artificial SOI. Our findings underscore the advantageous role of SOI in implementing long-range quantum information transfer protocols in quantum dot arrays, and show the feasibility of these systems as quantum links between processors for the transfer of quantum information, thus enhancing the quantum chip connectivity. Our results not only advance theoretical understanding of quantum systems with SOI but also pave the way for practical applications. The integration of simultaneous quantum gates into the transfer protocols offers the potential for significant acceleration of specific quantum information procedures.

ACKNOWLEDGMENTS

G.P. and D.F.F. are supported by Spain's MINECO through Grant No. PID2020-117787GB-I00 and by the CSIC Research Platform PTI-001. G.P. and D.F.F. also acknowledge the agreement between Carlos III University and the CSIC through the UA. D.F.F. acknowledges support from FPU Program No. FPU20/04762. Y.B. acknowledges support from the Spanish Government via the project PID2021-126694NA-C22 (MCIU/AEI/FEDER, EU).

Supplemental Material

EFFECTIVE SPIN-FLIP TUNNELING RATE

In germanium or silicon, the Dresselhaus spin-orbit interaction (SOI) vanishes because the system does not present BIA (bulk inversion asymmetry). Rashba interaction, due to SIA (structure inversion asymmetry), is the main SOI mechanism present in the material. Furthermore, depending on the sample configuration, the dominant term for Rashba SOI is linear or cubic in momentum [94–96]. Finally, this discussion can be extended to other semiconductor materials, such as GaAs.

The model for a double quantum dot (QD) in which heavy holes (HH) are confined along the out-of-plane (z) axis can be described by a quartic harmonic confining potential with dot separation $2a$. Additionally, there is an out-of-plane magnetic field B resulting in a Zeeman splitting for the spin degree of freedom. The Hamiltonian reads as follows

$$H_0 = \frac{\pi_x^2 + \pi_y^2}{2m^*} + \frac{1}{2}m^*\omega_0^2 \left(\frac{(x^2 - a^2)^2}{4a^2} + y^2 \right) + \frac{g}{2}\mu_B B \sigma_z, \quad (\text{SM1})$$

where $\boldsymbol{\pi} = \mathbf{p} + e\mathbf{A}$ is the canonical momentum and σ_i the Pauli matrices. The total Hamiltonian, taking into account Dresselhaus (β) and Rashba (α) SOI, both with linear and cubic terms, is described by $H = H_0 + H_{\text{SOI}}$, where $H_{\text{SOI}} \equiv H_\alpha^{(1)} + H_\alpha^{(3)} + H_\beta^{(1)} + H_\beta^{(3)}$ with

$$\begin{aligned} H_\alpha^{(1)} &= i\alpha^{(1)}(\sigma_- \pi_+ - \sigma_+ \pi_-), \\ H_\alpha^{(3)} &= i\alpha^{(3)}(\sigma_+ \pi_-^3 - \sigma_- \pi_+^3), \\ H_\beta^{(1)} &= \beta^{(1)}(\sigma_+ \pi_+ + \sigma_- \pi_-), \\ H_\beta^{(3)} &= \beta^{(3)}(\sigma_+ \pi_- \pi_+ \pi_- + \sigma_- \pi_+ \pi_- \pi_+). \end{aligned} \quad (\text{SM2})$$

The Hamiltonian in Eq. (SM1) can be exactly solved by obtaining the Fock-Darwin states $\psi_{nl}^{\text{FD}}(x, y)$. We will consider just a single orbital per dot, so we will restrict ourselves to $\psi_{00}^{\text{FD}}(x, y) = \frac{1}{\sqrt{\pi}b} \exp\{-(x^2 + y^2)/2b^2\}$, where we defined $b^2 \equiv \hbar/m^* \sqrt{\omega_0^2 + \omega_L^2}$, with the Larmor frequency $\omega_L = eB/2m^*$. The magnetic vector potential is defined in the symmetric gauge $\mathbf{A} = B(-y, x, 0)/2$. Transforming the Fock-Darwin states under this gauge, they acquire a phase as

$$\psi_{00}^{L/R} = e^{\pm iya/2l_B^2} \psi_{00}^{\text{FD}}(x \pm a, y). \quad (\text{SM3})$$

The finite overlap between the left and right wave functions is given by

$$S = \langle \psi_{00}^L | \psi_{00}^R \rangle = \exp\left(-\frac{a^2 m^* (\omega_0^2 + 2\omega_L^2)}{\hbar\omega}\right), \quad (\text{SM4})$$

with $\omega \equiv \sqrt{\omega_0^2 + \omega_L^2}$.

We orthogonalize the Wannier states as $|L/R\rangle = \sqrt{N}(\psi_{00}^{L/R} - \gamma\psi_{00}^{R/L})$, where the normalization is given by $N = (1 - 2\gamma S + \gamma^2)^{-1}$ and $\gamma = (1 - \sqrt{1 - S^2})/S$. The spin-flip terms for the SOI Hamiltonian are given by:

$$\begin{aligned} \langle L \downarrow | H_\alpha^{(1)} | R \uparrow \rangle &= -\alpha^{(1)} N (1 - \gamma^2) \frac{am^* \omega_0^2}{\omega} S, \\ \langle R \downarrow | H_\alpha^{(1)} | L \uparrow \rangle &= \alpha^{(1)} N (1 - \gamma^2) \frac{am^* \omega_0^2}{\omega} S, \end{aligned} \quad (\text{SM5})$$

$$\begin{aligned} \langle L \downarrow | H_\alpha^{(3)} | R \uparrow \rangle &= -\alpha^{(3)} N (1 - \gamma^2) \left(\frac{am^* \omega_0^2}{\omega} \right)^3 S, \\ \langle R \downarrow | H_\alpha^{(3)} | L \uparrow \rangle &= \alpha^{(3)} N (1 - \gamma^2) \left(\frac{am^* \omega_0^2}{\omega} \right)^3 S, \end{aligned} \quad (\text{SM6})$$

$$\begin{aligned}\langle L \downarrow | H_\beta^{(1)} | R \uparrow \rangle &= i\beta^{(1)} N(1 - \gamma^2) \frac{am^* \omega_0^2}{\omega} S, \\ \langle R \downarrow | H_\beta^{(1)} | L \uparrow \rangle &= -i\beta^{(1)} N(1 - \gamma^2) \frac{am^* \omega_0^2}{\omega} S,\end{aligned}\tag{SM7}$$

$$\begin{aligned}\langle L \downarrow | H_\beta^{(3)} | R \uparrow \rangle &= i\beta^{(3)} N(1 - \gamma^2) \frac{am^{*2} \omega_0^2}{\omega^3} (a^2 m^* \omega_0^4 - 2\hbar\omega(\omega_0^2 + 2\omega_L^2)) S, \\ \langle R \downarrow | H_\beta^{(3)} | L \uparrow \rangle &= -i\beta^{(3)} N(1 - \gamma^2) \frac{am^{*2} \omega_0^2}{\omega^3} (a^2 m^* \omega_0^4 - 2\hbar\omega(\omega_0^2 + 2\omega_L^2)) S.\end{aligned}\tag{SM8}$$

We computed $\langle L \downarrow | H_{\text{SOI}} | R \uparrow \rangle$ and $\langle R \downarrow | H_{\text{SOI}} | L \uparrow \rangle$, the other two matrix elements can be obtained by imposing the hermiticity of the resulting Hamiltonian. From Eqs. (SM5-SM8) we obtain that by including the linear or cubic term, both in the Rashba and Dresselhaus SOI terms, the phenomenology of the model remains the same, and the spin-flip tunneling rate can be written as

$$-\tau_F \equiv \langle R \downarrow | H_\beta^{(3)} | L \uparrow \rangle = -\langle L \downarrow | H_\beta^{(1)} + H_\beta^{(3)} | R \uparrow \rangle.\tag{SM9}$$

HAMILTONIAN FOR A TQD WITH ONE HOLE

The Hamiltonian given in Eq. (1) of the main text for a TQD, written on the basis of $\{|\uparrow, 0, 0\rangle, |0, \uparrow, 0\rangle, |0, 0, \uparrow\rangle, |\downarrow, 0, 0\rangle, |0, \downarrow, 0\rangle, |0, 0, \downarrow\rangle\}$, yields the following

$$H = \begin{pmatrix} \varepsilon_1 & -\tau_{C,1} & 0 & 0 & -\tau_{F,1} & 0 \\ -\tau_{C,1} & \varepsilon_2 & -\tau_{C,2} & \tau_{F,1} & 0 & -\tau_{F,2} \\ 0 & -\tau_{C,2} & \varepsilon_3 & 0 & \tau_{F,2} & 0 \\ 0 & \tau_{F,1} & 0 & \varepsilon_1 & -\tau_{C,1} & 0 \\ -\tau_{F,1} & 0 & \tau_{F,2} & -\tau_{C,1} & \varepsilon_2 & -\tau_{C,2} \\ 0 & -\tau_{F,2} & 0 & 0 & -\tau_{C,2} & \varepsilon_3 \end{pmatrix}.\tag{SM10}$$

EFFECTIVE MODEL FOR A QDA WITH $N > 3$

In this section, we obtain an effective model for a linear QD array (QDA) with more than three sites, populated with a single HH. To transfer the particle between the ends of the chain, we use straddling pulses, with all intermediate tunneling rates $\tau_{C,k}$, with $1 < k < N - 1$, equal to each other, see Fig. SM1. Setting $\tau_{F,k} = x_{\text{SOI}} \tau_{C,k}$, and after decoupling the leftmost and rightmost dots from the rest of the array $\tau_{C,1} = \tau_{C,N-1} = 0$, we obtain two dark states (DSs) described by

$$\begin{aligned}|\text{DS}_\uparrow\rangle &= \frac{1}{\sqrt{(N-1)/2}} \sum_{k=1}^{(N-1)/2} A_{2k-1} |\uparrow_{2k}\rangle - B_{2k-1} |\downarrow_{2k}\rangle, \\ |\text{DS}_\downarrow\rangle &= \frac{1}{\sqrt{(N-1)/2}} \sum_{k=1}^{(N-1)/2} B_{2k-1} |\uparrow_{2k}\rangle + A_{2k-1} |\downarrow_{2k}\rangle.\end{aligned}\tag{SM11}$$

Here, we have defined the functions

$$\begin{aligned}A_k &= (-1)^{(k+1)/2} \cos[\arctan(x_{\text{SOI}})(1-k)], \\ B_k &= (-1)^{(k+1)/2} \sin[\arctan(x_{\text{SOI}})(1-k)].\end{aligned}\tag{SM12}$$

In the limit of zero SOI, i.e., $x_{\text{SOI}} = 0$, the above expressions simplify as $A_i = (-1)^{(i+1)/2}$ and $B_i = 0$, obtaining the same DSs as those presented in [53], which only contain states with the same spin projection.

The DSs shown in Eq. (SM11) represent a dressed state formed by all the dots in the bulk of the QDA. We couple the edge QDs by setting $\tau_{C,1}, \tau_{C,2} \ll \tau_{C,k}$, which allows us to reduce the large QDA to an effective six-level system

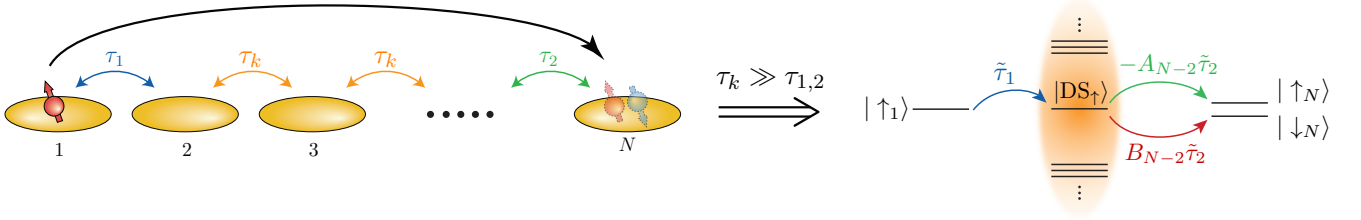


Figure SM1. Scheme of a linear N QDA, and straddling pulses τ_k applied to the intermediate dots. The system is initialized with a spin-up HH in the leftmost QD. Depending on the number of sites and the effective SOI, the transfer protocol conserves or inverts the spin of the particle. If the straddling pulse is much larger than the boundary pulses τ_1 and τ_2 , the dots in the bulk form a dressed state connecting the initial state with the final one. The effective coupling rate between the dressed and the final states depends on the functions A_k and B_k , which depend on the number of sites and the SOI ratio.

on the basis $\{|\uparrow_1\rangle, |\downarrow_1\rangle, |DS_\uparrow\rangle, |DS_\downarrow\rangle, |\uparrow_N\rangle, |\downarrow_N\rangle\}$

$$H = \begin{pmatrix} 0 & 0 & \tilde{\tau}_1(t) & 0 & 0 & 0 \\ 0 & 0 & 0 & \tilde{\tau}_1(t) & 0 & 0 \\ \tilde{\tau}_1(t) & 0 & 0 & 0 & -A_{N-2}\tilde{\tau}_2(t) & B_{N-2}\tilde{\tau}_2(t) \\ 0 & \tilde{\tau}_1(t) & 0 & 0 & B_{N-2}\tilde{\tau}_2(t) & A_{N-2}\tilde{\tau}_2(t) \\ 0 & 0 & -A_{N-2}\tilde{\tau}_2(t) & B_{N-2}\tilde{\tau}_2(t) & 0 & 0 \\ 0 & 0 & B_{N-2}\tilde{\tau}_2(t) & A_{N-2}\tilde{\tau}_2(t) & 0 & 0 \end{pmatrix}, \quad (\text{SM13})$$

with $\tilde{\tau}_{1(2)}(t) = \tau_{C,1(2)}(t)\sqrt{2/(N-1)}$. In the above equation, we have already used the fact that $A_1 = -1$ and $B_1 = 0$. This system can be identified with a QDA of three sites under transformation $|DS_{\uparrow(\downarrow)}\rangle \rightarrow |\uparrow(\downarrow)_2\rangle$. The final spin projection of the transferred particle depends on the number of sites in the total QDA and the value of the effective SOI. However, a long-range transfer with minimal population in the middle sites is possible even in large QDAs in the presence of SOI.

CHARGE NOISE

The success of quantum state transfer through a quantum bus hinges on its resilience against experimental errors throughout the protocol. In the context of HH spin qubits in semiconductor QDs, the most significant source of noise arises from electric field fluctuations, often referred to as charge noise.

We model charge noise by considering time-dependent fluctuations in both the energy of each QD and the barriers that define the tunneling rates. We parameterize the charge noise as [97]

$$\varepsilon_i^n(t) = \varepsilon_i + \delta_\varepsilon \nu_i(t), \quad (\text{SM14})$$

$$\tau_{C,i}^n(t) = \tau_{C,i}(t) + \delta_\tau \tilde{\nu}_i(t). \quad (\text{SM15})$$

Here, the superscript n indicates the presence of noise. Furthermore, we assume uncorrelated noise terms, which means there are no spatial correlations between them, with $\langle \nu_i(t)\nu_j(t) \rangle = \langle \tilde{\nu}_i(t)\tilde{\nu}_j(t) \rangle = \delta_{ij}$ and $\langle \tilde{\nu}_i(t)\nu_j(t) \rangle = 0$. To model charge noise, we employ a characteristic spectral density of pink noise, given by $S(f) \propto 1/f$ for frequencies within the range $f_{\min} < f < f_{\max}$. For frequencies below f_{\min} , we assume white noise without frequency dependence, and for frequencies above f_{\max} , we adopt Brownian noise with $S(f) \propto 1/f^2$. The parameters δ_ε and δ_τ represent the strength of the noise for detuning and tunneling rates, respectively. The spin-flip tunneling rates in the presence of noise are defined by the relation $\tau_{F,i}^n(t) = x_{\text{SOI}}\tau_{C,i}^n(t)$.

When simulating transfer under the influence of charge noise, the system is initialized at $|\Psi(0)\rangle = |\uparrow_1\rangle$. We then average the solution of the time-dependent Schrödinger equation over 10^3 independent noise realizations.

When charge noise is present due to fluctuations in the energy levels, Fig. SM2 (a), the highest fidelity for shorter times is obtained with STA. For larger times, CTAP and STA perform similarly to each other, obtaining a transfer fidelity close to $\mathcal{F} \sim 0.99$. However, the sequential protocol is more robust against charge noise (dashed brown curve), so if the total protocol time is long enough, such that the adiabatic condition is met, the fidelity is close to $\mathcal{F} \sim 0.999$. On the other hand, the linear ramp shows much worse results than the other ones. Linear ramps are very sensitive to charge noise in the energy levels and give rise to a maximum fidelity lower than 0.9.

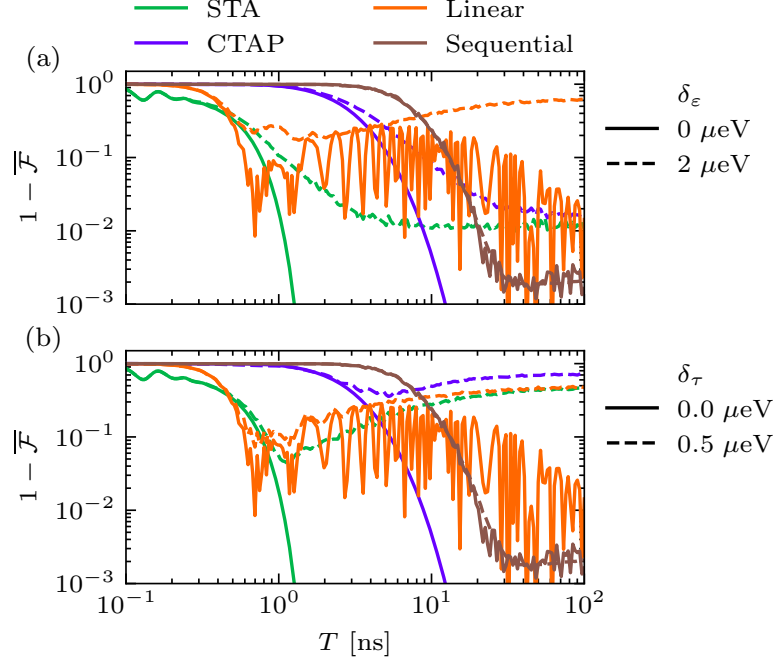


Figure SM2. Average infidelity of a long-range transfer in a seven QDA versus the total time of the protocol and (a) noise in the detuning, (b) noise in the tunneling rates. Each different protocol is represented with a color: STA (green), linear (orange), sequential (brown), and CTAP (purple). Solid lines represent zero noise, and dashed lines represent the infidelity in the presence of noise. $\tau_0 = 10 \mu\text{eV}$, $\tau_s = 10\tau_0$, $\varepsilon_{\text{max}} = 500 \mu\text{eV}$, $f_{\text{min}} = 0.16 \text{ mHz}$ and $f_{\text{max}} = 100 \text{ kHz}$.

Both CTAP and STA are much more sensitive to errors in tunneling rates, Fig. SM2 (b), obtaining fidelities lower than in the previous case. However, the sequential protocol is still robust against this error, obtaining fidelities close to the noiseless case.

In a more realistic case, more noise sources affect the system. Therefore, to improve the transfer fidelity, it is mandatory to perform the transfer as fast as possible. It is also beneficial for quantum algorithms to speed up the transfer between computing nodes, so the communication via quantum state transfer must be fast. A more detailed analysis of the different noise sources in a realistic set-up must be done to determine which protocol is more desirable.

DYNAMICAL DECOUPLING SCHEMES

In this section, we present the different protocols used for the dynamical decoupling schemes discussed in the main text. The schematics for the protocols are shown in Fig. SM3. In the sequential protocol, the particle is transported through all dots, and no quantum gate (or identity gate) is performed during the transfer. On the contrary, the direct transfer protocol implies that the middle dots are not populated, but dynamical decoupling is not applied. On the other hand, when the linear array is divided into three subarrays, we can perform different quantum gates during the transfer. In the first and third subarrays, we perform an $R_Y(\pi/2)$ rotation, and an $R_Y(\pi)$ rotation in the second one, performing a dynamical decoupling protocol in parallel to the particle transfer. We can also divide the total array into five subarrays, so the dynamical decoupling is applied during the first, third, and fifth subarrays. We benchmark the results of the dynamical decoupling schemes by performing a similar transfer in the absence of quantum gates applied during the transfer.

HALF-FILLING REGIME HAMILTONIAN

In this section, we will derive the effective Hamiltonian for a linear QDA in the half-filling regime with SOI, in the limit of high Coulomb interaction. To address this scenario, by means of a Schrieffer-Wolff transformation, we trace

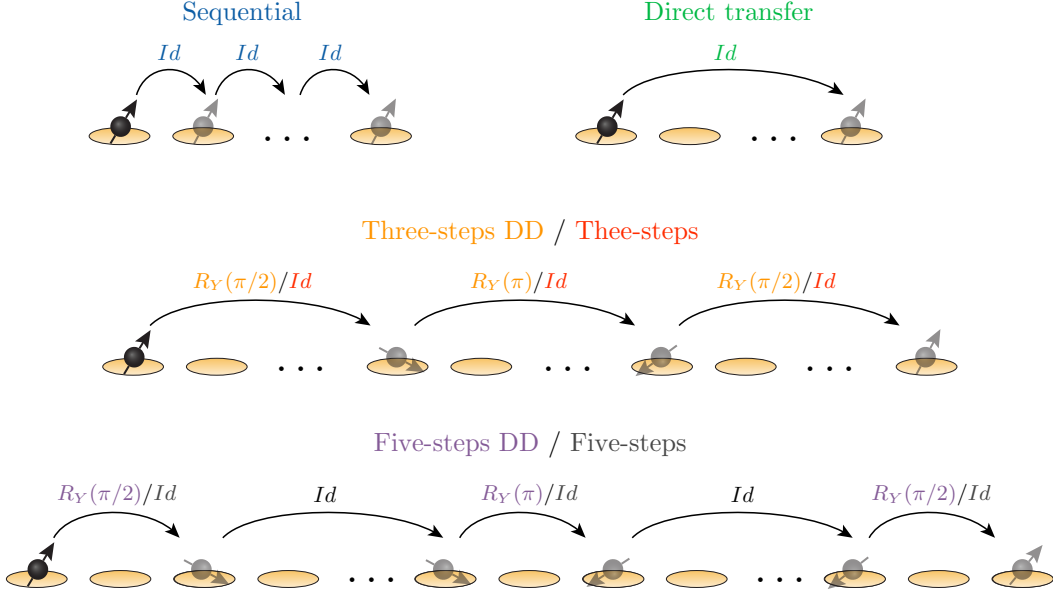


Figure SM3. Schematics of different long-range transfer protocols. During the transfer in the sequential and direct transfer protocols, no quantum gate is applied to the spin qubit, so no dynamical decoupling is performed. For the three- and five-steps protocols, if the identity quantum gate is applied (Id), then no dynamical decoupling is performed. On the other hand, if $R_y(\theta)$ is applied during each subarray transfer, then a dynamical decoupling (DD) protocol is executed.

out the double-occupied states, resulting in an effective exchange Hamiltonian. We consider a double QD populated with two HHs. In Fig. 10 of the main text, we illustrate the possible tunneling paths combining spin-conserving and spin-flip tunneling rates that a particle can perform in a DQD. The complete set of elements can be derived through spin inversion.

The original Hamiltonian H_0 is described in Eq. (2) of the main text. Both the spin-conserving tunneling term in Eq. (3), and the effective SOI in Eq. (4), are treated as perturbations to the original Hamiltonian via $V = H_\tau + H_{\text{SOI}}$. We perform a Schrieffer-Wolff transformation at first order, by solving: $V + [S, H_0] = 0$. In the next step, we simplify the effective model by considering $U \gg E_Z, \tau_{C,i}, \tau_{F,i}$. Finally, the effective Hamiltonian, for $\varepsilon_i = 0$, given by $H' = H_0 + [S, V]/2$, reads

$$\begin{aligned}
 H' = & E_Z(\sigma_z^1 + \sigma_z^2) + 2J^{CF}(\sigma_x^1\sigma_z^2 - \sigma_z^1\sigma_x^2) \\
 & + J^{CC}(\sigma_x^1\sigma_x^2 + \sigma_y^1\sigma_y^2 + \sigma_z^1\sigma_z^2 - 1/4) \\
 & + J^{FF}(-\sigma_x^1\sigma_x^2 + \sigma_y^1\sigma_y^2 - \sigma_z^1\sigma_z^2 - 1/4),
 \end{aligned} \tag{SM16}$$

where σ_α^i corresponds to the Pauli matrix $\alpha = \{x, y, z\}$ acting at the $i = \{1, 2\}$ site. The various exchange couplings are denoted as $J^{ab} \equiv \tau_a \tau_b / U$, where $a, b = \{C, F\}$ represent the spin-conserving and spin-flip tunneling rates, respectively. The effective model can be extended to longer arrays, with an arbitrary number of sites, as

$$\begin{aligned}
 H' = & E_Z \sum_i \sigma_z^i + 2 \sum_{\langle i,j \rangle} J_i^{CF} (\sigma_x^i \sigma_z^j - \sigma_z^i \sigma_x^j) \\
 & + \sum_{\langle i,j \rangle} J_i^{CC} (\sigma_x^i \sigma_x^j + \sigma_y^i \sigma_y^j + \sigma_z^i \sigma_z^j - 1/4) \\
 & + \sum_{\langle i,j \rangle} J_i^{FF} (-\sigma_x^i \sigma_x^j + \sigma_y^i \sigma_y^j - \sigma_z^i \sigma_z^j - 1/4).
 \end{aligned} \tag{SM17}$$

[1] D. Loss and D. P. DiVincenzo, Quantum computation with quantum dots, *Physical Review A* **57**, 120 (1998).

* david.fernandez@csic.es

- [2] G. Burkard, D. Loss, and D. P. DiVincenzo, Coupled quantum dots as quantum gates, *Physical Review B* **59**, 2070 (1999).
- [3] M. Ciorga, A. S. Sachrajda, P. Hawrylak, C. Gould, P. Zawadzki, S. Jullian, Y. Feng, and Z. Wasilewski, Addition spectrum of a lateral dot from coulomb and spin-blockade spectroscopy, *Physical Review B* **61**, R16315 (2000).
- [4] J. R. Petta, A. C. Johnson, J. M. Taylor, E. A. Laird, A. Yacoby, M. D. Lukin, C. M. Marcus, M. P. Hanson, and A. C. Gossard, Coherent Manipulation of Coupled Electron Spins in Semiconductor Quantum Dots, *Science* **309**, 2180 (2005).
- [5] K. C. Nowack, F. H. L. Koppens, Y. V. Nazarov, and L. M. K. Vandersypen, Coherent Control of a Single Electron Spin with Electric Fields, *Science* **318**, 1430 (2007).
- [6] S. Foletti, H. Bluhm, D. Mahalu, V. Umansky, and A. Yacoby, Universal quantum control of two-electron spin quantum bits using dynamic nuclear polarization, *Nature Physics* **5**, 903 (2009).
- [7] H. Bluhm, S. Foletti, I. Neder, M. Rudner, D. Mahalu, V. Umansky, and A. Yacoby, Dephasing time of GaAs electron-spin qubits coupled to a nuclear bath exceeding 200 μ s, *Nature Physics* **7**, 109 (2010).
- [8] A. Vidan, R. M. Westervelt, M. Stopa, M. Hanson, and A. C. Gossard, Triple quantum dot charging rectifier, *Applied Physics Letters* **85**, 3602 (2004).
- [9] L. Gaudreau, S. A. Studenikin, A. S. Sachrajda, P. Zawadzki, A. Kam, J. Lapointe, M. Korkusinski, and P. Hawrylak, Stability Diagram of a Few-Electron Triple Dot, *Physical Review Letters* **97**, 036807 (2006).
- [10] D. Schröer, A. D. Greentree, L. Gaudreau, K. Eberl, L. C. L. Hollenberg, J. P. Kotthaus, and S. Ludwig, Electrostatically defined serial triple quantum dot charged with few electrons, *Physical Review B* **76**, 075306 (2007).
- [11] M. C. Rogge and R. J. Haug, Two-path transport measurements on a triple quantum dot, *Physical Review B* **77**, 193306 (2008).
- [12] L. Gaudreau, G. Granger, A. Kam, G. C. Aers, S. A. Studenikin, P. Zawadzki, M. Pioro-Ladrière, Z. R. Wasilewski, and A. S. Sachrajda, Coherent control of three-spin states in a triple quantum dot, *Nature Physics* **8**, 54 (2011).
- [13] C. E. Creffield and G. Platero, Dynamical control of correlated states in a square quantum dot, *Physical Review B* **66**, 235303 (2002).
- [14] T. Hensgens, T. Fujita, L. Janssen, X. Li, C. J. V. Diepen, C. Reichl, W. Wegscheider, S. D. Sarma, and L. M. K. Vandersypen, Quantum simulation of a Fermi–Hubbard model using a semiconductor quantum dot array, *Nature* **548**, 70 (2017).
- [15] B. Pérez-González, M. Bello, G. Platero, and Á. Gómez-León, Simulation of 1D Topological Phases in Driven Quantum Dot Arrays, *Physical Review Letters* **123**, 126401 (2019).
- [16] J. P. Dehollain, U. Mukhopadhyay, V. P. Michal, Y. Wang, B. Wunsch, C. Reichl, W. Wegscheider, M. S. Rudner, E. Demler, and L. M. K. Vandersypen, Nagaoka ferromagnetism observed in a quantum dot plaquette, *Nature* **579**, 528 (2020).
- [17] C. van Diepen, T.-K. Hsiao, U. Mukhopadhyay, C. Reichl, W. Wegscheider, and L. Vandersypen, Quantum Simulation of Antiferromagnetic Heisenberg Chain with Gate-Defined Quantum Dots, *Physical Review X* **11**, 041025 (2021).
- [18] X. Xue, M. Russ, N. Samkharadze, B. Undseth, A. Sammak, G. Scappucci, and L. M. K. Vandersypen, Quantum logic with spin qubits crossing the surface code threshold, *Nature* **601**, 343 (2022).
- [19] M. Busl, R. Sánchez, and G. Platero, Control of spin blockade by ac magnetic fields in triple quantum dots, *Physical Review B* **81**, 121306 (2010).
- [20] R. Sánchez, G. Granger, L. Gaudreau, A. Kam, M. Pioro-Ladrière, S. Studenikin, P. Zawadzki, A. Sachrajda, and G. Platero, Long-range spin transfer in triple quantum dots, *Physical Review Letters* **112**, 176803 (2014).
- [21] F. R. Braakman, P. Barthelemy, C. Reichl, W. Wegscheider, and L. M. K. Vandersypen, Long-distance coherent coupling in a quantum dot array, *Nature Nanotechnology* **8**, 432 (2013).
- [22] F. Gallego-Marcos, R. Sánchez, and G. Platero, Photon assisted long-range tunneling, *Journal of Applied Physics* **117**, 10.1063/1.4913834 (2015).
- [23] J. Picó-Cortés, F. Gallego-Marcos, and G. Platero, Direct transfer of two-electron quantum states in ac-driven triple quantum dots, *Physical Review B* **99**, 155421 (2019).
- [24] J. Picó-Cortés and G. Platero, Dynamical second-order noise sweetspots in resonantly driven spin qubits, *Quantum* **5**, 607 (2021).
- [25] D. Zajac, T. Hazard, X. Mi, E. Nielsen, and J. Petta, Scalable Gate Architecture for a One-Dimensional Array of Semiconductor Spin Qubits, *Physical Review Applied* **6**, 054013 (2016).
- [26] T. Otsuka, T. Nakajima, M. R. Delbecq, S. Amaha, J. Yoneda, K. Takeda, G. Allison, T. Ito, R. Sugawara, A. Noiri, A. Ludwig, A. D. Wieck, and S. Tarucha, Single-electron Spin Resonance in a Quadruple Quantum Dot, *Scientific Reports* **6**, 10.1038/srep31820 (2016).
- [27] T. A. Baart, M. Shafiei, T. Fujita, C. Reichl, W. Wegscheider, and L. M. K. Vandersypen, Single-spin CCD, *Nature Nanotechnology* **11**, 330 (2016).
- [28] T. Fujita, T. A. Baart, C. Reichl, W. Wegscheider, and L. M. K. Vandersypen, Coherent shuttle of electron-spin states, *npj Quantum Information* **3**, 10.1038/s41534-017-0024-4 (2017).
- [29] Y. P. Kandel, H. Qiao, S. Fallahi, G. C. Gardner, M. J. Manfra, and J. M. Nichol, Coherent spin-state transfer via Heisenberg exchange, *Nature* **573**, 553 (2019).
- [30] H. Qiao, Y. P. Kandel, S. K. Manikandan, A. N. Jordan, S. Fallahi, G. C. Gardner, M. J. Manfra, and J. M. Nichol, Conditional teleportation of quantum-dot spin states, *Nature Communications* **11**, 10.1038/s41467-020-16745-0 (2020).
- [31] W. I. L. Lawrie, H. G. J. Eenink, N. W. Hendrickx, J. M. Boter, L. Petit, S. V. Amitonov, M. Lodari, B. P. Wuetz, C. Volk, S. G. J. Philips, G. Droulers, N. Kalthor, F. van Riggelen, D. Brousse, A. Sammak, L. M. K. Vandersypen, G. Scappucci, and M. Veldhorst, Quantum dot arrays in silicon and germanium, *Applied Physics Letters* **116**, 10.1063/5.0002013 (2020).
- [32] C. X. Yu, S. Zihlmann, J. C. Abadillo-Uriel, V. P. Michal, N. Rambal, H. Niebojewski, T. Bedecarrats, M. Vinet, É. Dumur, M. Filippone, B. Bertrand, S. D. Franceschi, Y.-M. Niquet, and R. Maurand, Strong coupling between a photon and a hole spin in silicon, *Nature Nanotechnology* **18**, 741 (2023).
- [33] T. Nguyen, C. D. Hill, L. C. L. Hollenberg, and M. R.

- James, Fan-out Estimation in Spin-based Quantum Computer Scale-up, *Scientific Reports* **7**, [10.1038/s41598-017-13308-0](https://doi.org/10.1038/s41598-017-13308-0) (2017).
- [34] S. J. Pauka, K. Das, R. Kalra, A. Moini, Y. Yang, M. Trainer, A. Bousquet, C. Cantaloube, N. Dick, G. C. Gardner, M. J. Manfra, and D. J. Reilly, Cryogenic Interface for Controlling Many Qubits (2019), [arXiv:1912.01299](https://arxiv.org/abs/1912.01299) [quant-ph].
- [35] R. Li, L. Petit, D. P. Franke, J. P. Dehollain, J. Helsen, M. Steudtner, N. K. Thomas, Z. R. Yoscovits, K. J. Singh, S. Wehner, L. M. K. Vandersypen, J. S. Clarke, and M. Veldhorst, A crossbar network for silicon quantum dot qubits, *Science Advances* **4**, [10.1126/sciadv.aar3960](https://doi.org/10.1126/sciadv.aar3960) (2018).
- [36] J. M. Boter, J. P. Dehollain, J. P. van Dijk, Y. Xu, T. Hensgens, R. Versluis, H. W. Naus, J. S. Clarke, M. Veldhorst, F. Sebastiano, and L. M. Vandersypen, Spiderweb Array: A Sparse Spin-Qubit Array, *Physical Review Applied* **18**, 024053 (2022).
- [37] L. M. K. Vandersypen, H. Bluhm, J. S. Clarke, A. S. Dzurak, R. Ishihara, A. Morello, D. J. Reilly, L. R. Schreiber, and M. Veldhorst, Interfacing spin qubits in quantum dots and donors—hot, dense, and coherent, *npj Quantum Information* **3**, [10.1038/s41534-017-0038-y](https://doi.org/10.1038/s41534-017-0038-y) (2017).
- [38] B. Buonacorsi, Z. Cai, E. B. Ramirez, K. S. Willick, S. M. Walker, J. Li, B. D. Shaw, X. Xu, S. C. Benjamin, and J. Baugh, Network architecture for a topological quantum computer in silicon, *Quantum Science and Technology* **4**, 025003 (2019).
- [39] H. Jnane, B. Undseth, Z. Cai, S. C. Benjamin, and B. Koczor, Multicore Quantum Computing, *Physical Review Applied* **18**, 044064 (2022).
- [40] M. Künne, A. Willmes, M. Oberländer, C. Gorjaew, J. D. Teske, H. Bhardwaj, M. Beer, E. Kammerloher, R. Otten, I. Seidler, R. Xue, L. R. Schreiber, and H. Bluhm, The SpinBus Architecture: Scaling Spin Qubits with Electron Shuttling (2023), [arXiv:2306.16348](https://arxiv.org/abs/2306.16348) [quant-ph].
- [41] P. Harvey-Collard, J. Dijkema, G. Zheng, A. Sammak, G. Scappucci, and L. M. Vandersypen, Coherent Spin-Spin Coupling Mediated by Virtual Microwave Photons, *Physical Review X* **12**, 021026 (2022).
- [42] J. M. Shilton, V. I. Talyanskii, M. Pepper, D. A. Ritchie, J. E. F. Frost, C. J. B. Ford, C. G. Smith, and G. A. C. Jones, High-frequency single-electron transport in a quasi-one-dimensional GaAs channel induced by surface acoustic waves, *Journal of Physics: Condensed Matter* **8**, L531 (1996).
- [43] A. R. Mills, D. M. Zajac, M. J. Gullans, F. J. Schupp, T. M. Hazard, and J. R. Petta, Shuttling a single charge across a one-dimensional array of silicon quantum dots, *Nature Communications* **10**, [10.1038/s41467-019-08970-z](https://doi.org/10.1038/s41467-019-08970-z) (2019).
- [44] F. van Riggelen-Doelman, C.-A. Wang, S. L. de Snoo, W. I. L. Lawrie, N. W. Hendrickx, M. Rimbach-Russ, A. Sammak, G. Scappucci, C. Déprez, and M. Veldhorst, Coherent spin qubit shuttling through germanium quantum dots, [arXiv 2308.02406](https://arxiv.org/abs/2308.02406) (2023).
- [45] A. Zwerver, S. Amitonov, S. de Snoo, M. Mądzik, M. Rimbach-Russ, A. Sammak, G. Scappucci, and L. Vandersypen, Shuttling an electron spin through a silicon quantum dot array, *PRX Quantum* **4**, 030303 (2023).
- [46] I. Seidler, T. Struck, R. Xue, N. Focke, S. Trellenkamp, H. Bluhm, and L. R. Schreiber, Conveyor-mode single-electron shuttling in Si/SiGe for a scalable quantum computing architecture, *npj Quantum Information* **8**, [10.1038/s41534-022-00615-2](https://doi.org/10.1038/s41534-022-00615-2) (2022).
- [47] T. Struck, M. Volmer, L. Visser, T. Offermann, R. Xue, J.-S. Tu, S. Trellenkamp, Łukasz Cywiński, H. Bluhm, and L. R. Schreiber, Spin-EPR-pair separation by conveyor-mode single electron shuttling in Si/SiGe (2023), [arXiv:2307.04897](https://arxiv.org/abs/2307.04897) [quant-ph].
- [48] Veit Langrock and Jan A. Krzywda and Niels Focke and Inga Seidler and Lars R. Schreiber and Łukasz Cywiński, Blueprint of a Scalable Spin Qubit Shuttling Device for Coherent Mid-Range Qubit Transfer in Disordered Si/SiGe/SiO₂, *PRX Quantum* **4**, 020305 (2023).
- [49] R. Xue, M. Beer, I. Seidler, S. Humpohl, J.-S. Tu, S. Trellenkamp, T. Struck, H. Bluhm, and L. R. Schreiber, Si/SiGe QuBus for single electron information-processing devices with memory and micron-scale connectivity function (2023), [arXiv:2306.16375](https://arxiv.org/abs/2306.16375) [cond-mat.mes-hall].
- [50] A. D. Greentree, J. H. Cole, A. R. Hamilton, and L. C. L. Hollenberg, Coherent electronic transfer in quantum dot systems using adiabatic passage, *Physical Review B* **70**, 235317 (2004).
- [51] Y. Ban, X. Chen, and G. Platero, Fast long-range charge transfer in quantum dot arrays, *Nanotechnology* **29**, 505201 (2018).
- [52] Y. Ban, X. Chen, S. Kohler, and G. Platero, Spin Entangled State Transfer in Quantum Dot Arrays: Coherent Adiabatic and Speed-Up Protocols, *Advanced Quantum Technologies* **2**, 1900048 (2019).
- [53] M. J. Gullans and J. R. Petta, Coherent transport of spin by adiabatic passage in quantum dot arrays, *Physical Review B* **102**, 155404 (2020).
- [54] A. Bogan, S. Studenikin, M. Korkusinski, G. Aers, L. Gaudreau, P. Zawadzki, A. Sachrajda, L. Tracy, J. Reno, and T. Hargett, Consequences of spin-orbit coupling at the single hole level: Spin-flip tunneling and the anisotropic g factor, *Physical Review Letters* **118**, 167701 (2017).
- [55] A. Bogan, S. Studenikin, M. Korkusinski, L. Gaudreau, P. Zawadzki, A. S. Sachrajda, L. Tracy, J. Reno, and T. Hargett, Landau-Zener-Stückelberg-Majorana Interferometry of a Single Hole, *Physical Review Letters* **120**, 207701 (2018).
- [56] S. Studenikin, M. Korkusinski, M. Takahashi, J. Ducatel, A. Padawer-Blatt, A. Bogan, D. G. Austing, L. Gaudreau, P. Zawadzki, A. Sachrajda, Y. Hirayama, L. Tracy, J. Reno, and T. Hargett, Electrically tunable effective g -factor of a single hole in a lateral GaAs/AlGaAs quantum dot, *Communications Physics* **2**, [10.1038/s42005-019-0262-1](https://doi.org/10.1038/s42005-019-0262-1) (2019).
- [57] A. Bogan, S. Studenikin, M. Korkusinski, L. Gaudreau, P. Zawadzki, A. Sachrajda, L. Tracy, J. Reno, and T. Hargett, Single hole spin relaxation probed by fast single-shot latched charge sensing, *Communications Physics* **2**, [10.1038/s42005-019-0113-0](https://doi.org/10.1038/s42005-019-0113-0) (2019).
- [58] S. Studenikin, M. Korkusinski, A. Bogan, L. Gaudreau, D. G. Austing, A. S. Sachrajda, L. Tracy, J. Reno, and T. Hargett, Single-hole physics in GaAs/AlGaAs double quantum dot system with strong spin-orbit interaction, *Semiconductor Science and Technology* **36**, 053001 (2021).
- [59] J. Ducatel, A. Padawer-Blatt, A. Bogan, M. Korkusinski, P. Zawadzki, A. Sachrajda, S. Studenikin, L. Tracy, J. Reno, and T. Hargett, Single-hole couplings in GaAs/AlGaAs double dots probed with trans-

- port and edsr spectroscopy, *Applied Physics Letters* **118**, 10.1063/5.0044933 (2021).
- [60] A. Bogan, S. Studenikin, M. Korkusinski, L. Gaudreau, J. Phoenix, P. Zawadzki, A. Sachrajda, L. Tracy, J. Reno, and T. Hargett, Spin-orbit enabled quantum transport channels in a two-hole double quantum dot, *Physical Review B* **103**, 235310 (2021).
- [61] A. Padawer-Blatt, J. Ducatel, M. Korkusinski, A. Bogan, L. Gaudreau, P. Zawadzki, D. G. Austing, A. S. Sachrajda, S. Studenikin, L. Tracy, J. Reno, and T. Hargett, Characterization of dot-specific and tunable effective g factors in a gaas/algaas double quantum dot single-hole device, *Physical Review B* **105**, 195305 (2022).
- [62] V. Marton, A. Sachrajda, M. Korkusinski, A. Bogan, and S. Studenikin, Coherence characteristics of a gaas single heavy-hole spin qubit using a modified single-shot latching readout technique, *Nanomaterials* **13**, 950 (2023).
- [63] F. Ginzler, A. R. Mills, J. R. Petta, and G. Burkard, Spin shuttling in a silicon double quantum dot, *Physical Review B* **102**, 195418 (2020).
- [64] J. Qi, Z.-H. Liu, and H. Q. Xu, Spin-Orbit Interaction Enabled High-Fidelity Two-Qubit Gates (2023), [arXiv:2308.06986 \[cond-mat.mes-hall\]](https://arxiv.org/abs/2308.06986).
- [65] D. Guéry-Odelin, A. Ruschhaupt, A. Kiely, E. Torrontegui, S. Martínez-Garaot, and J. Muga, Shortcuts to adiabaticity: Concepts, methods, and applications, *Reviews of Modern Physics* **91**, 045001 (2019).
- [66] Y. Fang, P. Philippopoulos, D. Culcer, W. A. Coish, and S. Chesì, Recent advances in hole-spin qubits, *Materials for Quantum Technology* **3**, 012003 (2023).
- [67] D. Fernández-Fernández, Y. Ban, and G. Platero, Quantum Control of Hole Spin Qubits in Double Quantum Dots, *Physical Review Applied* **18**, 054090 (2022).
- [68] D. Fernández-Fernández, J. Picó-Cortés, S. V. Liñán, and G. Platero, Photo-assisted spin transport in double quantum dots with spin-orbit interaction, *Journal of Physics: Materials* **6**, 034004 (2023).
- [69] G. Burkard, T. D. Ladd, A. Pan, J. M. Nichol, and J. R. Petta, Semiconductor spin qubits, *Reviews of Modern Physics* **95**, 025003 (2023).
- [70] P. M. Mutter and G. Burkard, Cavity control over heavy-hole spin qubits in inversion-symmetric crystals, *Physical Review B* **102**, 205412 (2020).
- [71] S. Bosco, M. Benito, C. Adelsberger, and D. Loss, Squeezed hole spin qubits in Ge quantum dots with ultrafast gates at low power, *Physical Review B* **104**, 115425 (2021).
- [72] P. M. Mutter and G. Burkard, All-electrical control of hole singlet-triplet spin qubits at low-leakage points, *Physical Review B* **104**, 195421 (2021).
- [73] P. M. Mutter and G. Burkard, Natural heavy-hole flopping mode qubit in germanium, *Physical Review Research* **3**, 013194 (2021).
- [74] C. Adelsberger, M. Benito, S. Bosco, J. Klinovaja, and D. Loss, Hole-spin qubits in Ge nanowire quantum dots: Interplay of orbital magnetic field, strain, and growth direction, *Physical Review B* **105**, 075308 (2022).
- [75] D. Jirovec, P. M. Mutter, A. Hofmann, A. Crippa, M. Rychetsky, D. L. Craig, J. Kukucka, F. Martins, A. Ballabio, N. Ares, D. Chrastina, G. Isella, G. Burkard, and G. Katsaros, Dynamics of Hole Singlet-Triplet Qubits with Large g -Factor Differences, *Physical Review Letters* **128**, 126803 (2022).
- [76] P. M. Mutter and G. Burkard, Pauli spin blockade with site-dependent g tensors and spin-polarized leads, *Physical Review B* **103**, 245412 (2021).
- [77] X. Chen, A. Ruschhaupt, S. Schmidt, A. del Campo, D. Guéry-Odelin, and J. G. Muga, Fast Optimal Frictionless Atom Cooling in Harmonic Traps: Shortcut to Adiabaticity, *Physical Review Letters* **104**, 063002 (2010).
- [78] V. S. Malinovsky and D. J. Tannor, Simple and robust extension of the stimulated raman adiabatic passage technique to n -level systems, *Physical Review A* **56**, 4929 (1997).
- [79] N. Vitanov, M. Fleischhauer, B. Shore, and K. Bergmann, Coherent Manipulation of Atoms Molecules By Sequential Laser Pulses, in *Advances In Atomic, Molecular, and Optical Physics* (Elsevier, 2001) pp. 55–190.
- [80] D. Manzano, A short introduction to the lindblad master equation, *AIP Advances* **10**, 10.1063/1.5115323 (2020).
- [81] J. Nitta, T. Akazaki, H. Takayanagi, and T. Enoki, Gate control of spin-orbit interaction in an inverted $\text{In}_{0.53}\text{Ga}_{0.47}\text{As}/\text{In}_{0.52}\text{Al}_{0.48}\text{As}$ heterostructure, *Phys. Rev. Lett.* **78**, 1335 (1997).
- [82] A. G. Mal'shukov, C. S. Tang, C. S. Chu, and K. A. Chao, Spin-current generation and detection in the presence of an ac gate, *Physical Review B* **68**, 233307 (2003).
- [83] S. Faniel, T. Matsuura, S. Mineshige, Y. Sekine, and T. Koga, Determination of spin-orbit coefficients in semiconductor quantum wells, *Physical Review B* **83**, 115309 (2011).
- [84] Y.-C. Li, X. Chen, J. G. Muga, and E. Y. Sherman, Qubit gates with simultaneous transport in double quantum dots, *New Journal of Physics* **20**, 113029 (2018).
- [85] A. Barenco, C. H. Bennett, R. Cleve, D. P. DiVincenzo, N. Margolus, P. Shor, T. Sleator, J. A. Smolin, and H. Weinfurter, Elementary gates for quantum computation, *Physical Review A* **52**, 3457 (1995).
- [86] Y.-P. Shim, J. Fei, S. Oh, X. Hu, and M. Friesen, Single-qubit gates in two steps with rotation axes in a single plane (2013), [arXiv:1303.0297 \[cond-mat.mes-hall\]](https://arxiv.org/abs/1303.0297).
- [87] P. Stano and D. Loss, Review of performance metrics of spin qubits in gated semiconducting nanostructures, *Nature Reviews Physics* **4**, 672 (2022).
- [88] W. Huang, C. H. Yang, K. W. Chan, T. Tanttu, B. Hensen, R. C. C. Leon, M. A. Fogarty, J. C. C. Hwang, F. E. Hudson, K. M. Itoh, A. Morello, A. Laucht, and A. S. Dzurak, Fidelity benchmarks for two-qubit gates in silicon, *Nature* **569**, 532 (2019).
- [89] N. W. Hendrickx, W. I. L. Lawrie, M. Russ, F. van Riggenlen, S. L. de Snoo, R. N. Schouten, A. Sammak, G. Scappucci, and M. Veldhorst, A four-qubit germanium quantum processor, *Nature* **591**, 580 (2021).
- [90] L. V. C. Assali, H. M. Petrilli, R. B. Capaz, B. Koiller, X. Hu, and S. D. Sarma, Hyperfine interactions in silicon quantum dots, *Physical Review B* **83**, 165301 (2011).
- [91] H. Y. Carr and E. M. Purcell, Effects of diffusion on free precession in nuclear magnetic resonance experiments, *Physical Review* **94**, 630 (1954).
- [92] S. Meiboom and D. Gill, Modified spin-echo method for measuring nuclear relaxation times, *Review of Scientific Instruments* **29**, 688 (1958).
- [93] N. V. Vitanov, A. A. Rangelov, B. W. Shore, and K. Bergmann, Stimulated Raman adiabatic passage in physics, chemistry, and beyond, *Reviews of Modern Physics* **89**, 015006 (2017).
- [94] J.-W. Luo, A. N. Chantis, M. van Schilfhaarde, G. Bester,

- and A. Zunger, Discovery of a novel linear-in- k spin splitting for holes in the 2d GaAs/AlAs system, *Physical Review Letters* **104**, 066405 (2010).
- [95] P. Szumniak, S. Bednarek, B. Partoens, and F. M. Peeters, Spin-Orbit-Mediated Manipulation of Heavy-Hole Spin Qubits in Gated Semiconductor Nanodevices, *Physical Review Letters* **109**, 107201 (2012).
- [96] Y. Liu, J.-X. Xiong, Z. Wang, W.-L. Ma, S. Guan, J.-W. Luo, and S.-S. Li, Emergent linear Rashba spin-orbit coupling offers fast manipulation of hole-spin qubits in germanium, *Physical Review B* **105**, 075313 (2022).
- [97] M. J. Gullans and J. R. Petta, Protocol for a resonantly driven three-qubit Toffoli gate with silicon spin qubits, *Physical Review B* **100**, 085419 (2019).